3D printing microporous scaffolds from modular bioinks containing sacrificial, cell-encapsulating microgels

Journal:	*Biomaterials Science*
Manuscript ID	BM-ART-04-2023-000721.R1
Article Type:	Paper
Date Submitted by the Author:	05-Sep-2023
Complete List of Authors:	Seymour, Alexis; Stanford University, Bioengineering Kilian, David; Stanford University, Materials Science & Engineering Navarro, Renato; Stanford University Hull, Sarah M; Stanford University Heilshorn, Sarah; Stanford University School of Engineering, Materials Science and Engineering

3D Printing Microporous Scaffolds from Modular Bioinks Containing Sacrificial, Cell-Encapsulating Microgels

*Alexis J. Seymour, David Kilian, Renato S. Navarro, Sarah M. Hull, and Sarah C. Heilshorn**

A. J. Seymour
Department of Bioengineering, Stanford University, Stanford, CA 94305, USA

D. Kilian, R. S. Navarro, Prof. S. C. Heilshorn
Department of Materials Science & Engineering, Stanford University, Stanford, CA 94305, USA
E-mail: heilshorn@stanford.edu

S. M. Hull
Department of Chemical Engineering, Stanford University, Stanford, CA 94305, USA

Keywords: 3D printing, microgels, granular ink, void fraction, gelatin methacryloyl, oxidized alginate, endothelial cells

Abstract

Microgel-based biomaterials have inherent porosity and are often extrudable, making them well-suited for 3D bioprinting applications. Cells are commonly introduced into these granular inks post-printing using cell infiltration. However, due to slow cell migration speeds, this strategy struggles to achieve depth-independent cell distributions within thick 3D printed geometries. To address this, we leverage granular ink modularity by combining two microgels with distinct functions: (1) structural, UV-crosslinkable microgels made from gelatin methacryloyl (GelMA) and (2) sacrificial, cell-laden microgels made from oxidized alginate (AlgOx). We hypothesize that encapsulating cells within sacrificial AlgOx microgels would enable the simultaneous introduction of void space and release of cells at depths unachievable through cell infiltration alone. Blending the microgels in different ratios produces a family of highly printable GelMA:AlgOx microgel inks with void fractions ranging from 0.03 to 0.35. As expected, void fraction influences the morphology of human umbilical vein endothelial cells (HUVEC) within GelMA:AlgOx inks. Crucially, void fraction does not alter the ideal HUVEC distribution seen throughout the depth of 3D printed samples. This work presents a strategy for fabricating constructs with tunable porosity and depth-independent cell distribution, highlighting the promise of microgel-based inks for 3D bioprinting.

1. Introduction

Three-dimensional (3D) bioprinting strives to scalably create complex, functional tissue mimics to better understand and treat human disease.[1-5] Toward this goal, bioprinting uses biomaterials, such as hydrogels, as inks to fabricate biologically-relevant 3D constructs.[6] The chosen fabrication approach imposes viscoelastic requirements on the biomaterial ink. For example, additive manufacturing via extrusion-based bioprinting necessitates the use of inks that are shear-thinning and self-healing, two properties that enable ink deposition (or 'extrusion') and promote printed shape accuracy (or 'fidelity').[7, 8] When blended with cells, the biomaterial ink becomes a 'bioink' that serves as both a physical scaffold and an instructive cell niche.[6] Using widely-studied biopolymers as inks provides the opportunity to leverage knowledge from biomaterials science for application-specific modulation of viscoelastic properties and microenvironmental characteristics. However, tradeoffs often must be made between optimizing the ink for either biofabrication or cell support.[1, 2, 7, 9]

Granular inks composed of hydrogel microparticles (i.e., 'microgels') can readily satisfy the viscoelastic requirements of extrusion-based biofabrication while simultaneously enabling tuning of the cellular microenvironment. Though granular hydrogels display solid-like viscoelastic properties at sufficient packing densities, these jammed microgel slurries are held together by noncovalent, frictional, and electrostatic interparticle forces that can be disrupted by and reform after the application of shear force.[10-13] This emergent macroscale behavior makes granular hydrogels ideal for extrusion-mediated biofabrication strategies. Microgel-based inks can also be modular, meaning that multiple microgel populations with unique functions can be blended into one granular ink to confer desirable traits upon the printed construct.[14, 15] Furthermore, due to microgel geometry, granular hydrogels inherently contain interparticle microporosity. The void space imparted by these interconnected pores has been shown to promote greater cell viability, proliferation, and infiltration when compared to homogeneous bulk hydrogels with nanoscale porosity.[16-21] The beneficial effect of porosity on these important cell outcomes makes introducing and controlling void space within hydrogel-based biomaterials a pervasive goal for tissue-engineered constructs.[22, 23] Several strategies have been developed to achieve this goal in granular hydrogels. For example, the size and shape of interparticle voids can be altered through microgel diameter or aspect ratio.[17, 24-27] Meanwhile, the total void fraction within granular hydrogels has been controlled by altering microgel packing density through microgel concentration.[26, 28] Recent work, however, demonstrated that microgel concentration is inseparably tied to the viscoelastic properties, and therefore printability, of granular hydrogel inks used for 3D bioprinting.[18] Specifically, increasing this beneficial void fraction by lowering microgel concentration results in poor shape fidelity.

Previously, we leveraged microgel modularity to enable user-defined control of void fraction independent of ink printability by blending crosslinkable and sacrificial microgels.[18] While this work provided a flexible strategy to expand granular ink printability, it relied upon void fraction-mediated cell migration from the sample surface to populate printed constructs. Though promising for some in vivo applications, this cell-infiltration-dependent approach is insufficient for the successful cellularization of thick 3D printed tissue constructs due to slow cell migration speeds.[29, 30] Instead, cells can be introduced throughout granular hydrogels before 3D printing in two ways: **(1)** by mixing cells into interparticle voids or **(2)** by directly encapsulating cells within the microgels.[12, 15, 17, 26, 27, 31-33] While encapsulating cells within microgels can protect them from the high-shear-stress environment experienced during bioprinting, this approach still suffers from the restricted cell motility seen in bulk hydrogels due to the slow degradation rates of the microgels used. Furthermore, no studies have explored strategies to control void fraction independent of printability within cell-encapsulating microgel-based bioinks to date.

Here we design a new family of modular, granular bioinks to enable the rapid cellularization of thick 3D constructs with tunable internal porosity. Specifically, we hypothesized that encapsulating cells within sacrificial microgels would confer control over scaffold void fraction while attaining a depth-independent distribution of cells throughout the 3D printed samples. To this end, we mixed structural, photocrosslinkable microgels with sacrificial, cell-containing microgels. The ratio of each microgel component was altered from 100% structural (100:0) to 100% sacrificial (0:100) by weight to tune the post-print void fraction. Inks with at least 50% structural microgel content (100:0 through 50:50) remained stably crosslinked after sacrificial microgel dissolution. The shape fidelity of printed lattices was similar across all formulations. Crucially, the introduction of sacrificial microgels produced a family of inks containing multiscale porosity with total void fractions ranging from 0.03 ± 0.02 to 0.35 ± 0.07. Despite sacrificial, cell-containing microgel content ranging from 10% to 50%, constructs printed from these two-component bioinks had similarly uniform cell distributions across representative 200-µm-thick vertical sections. Together, these findings demonstrate that direct encapsulation and printing of cells within sacrificial microgels enables the introduction of beneficial void space while accelerating cell delivery deep within a printed construct.

2. Results and Discussion

2.1. Design of Granular GelMA:AlgOx Microgel Inks

We used a two-component granular ink to address the need for both rapid cellularization of printed constructs and control over internal void fraction. The first component was a structural microgel that undergoes covalent crosslinking after 3D printing to maintain the mechanical integrity of the printed shape. This component also served as a substrate for cell growth. The second component was a sacrificial microgel used as a bulking agent and cell carrier during printing and as a porogen after printing to introduce greater void space into the printed construct. Human umbilical vein endothelial cells (HUVEC) were used as a model cell type and were encapsulated within the sacrificial microgels to enable degradation-mediated cell release. This required the sacrificial microgels to be created using a cytocompatible fabrication strategy and rapidly biodegradable materials.

Gelatin methacryloyl (GelMA), a widely used biomaterial, was employed to create the structural microgels.[18, 20, 34] Before microgel fabrication, the naturally-derived biopolymer gelatin was modified with methacrylic anhydride (MAA) using a one-pot method as previously described.[35, 36] Successful gelatin modification was validated using nuclear magnetic resonance (^{1}H NMR) analysis and indicated a degree of substitution of ~ 47% (**Figure S1**, Supporting Information). With this degree of substitution, the GelMA retained its ability to undergo thermal gelation while enabling triggerable covalent photocrosslinking with ultraviolet (UV) light. We leveraged this thermal crosslinking to produce GelMA microgels using mechanical fragmentation via extrusion.[37, 38] Briefly, a GelMA precursor hydrogel was cast within a syringe at 4 °C. Once solidified, the precursor hydrogel was fragmented by extrusion through blunt-end needles with inner diameters (*ID*) decreasing from 965 µm (18-gauge) to 160 µm (30-gauge) (**Figure 1**A, left). The resulting microgels had heterogeneous diameters and irregular, jagged shapes, consistent with production using fragmentation-based approaches (Figure 1B, left).[5, 37] Specifically, the equivalent diameter of structural GelMA microgels ranged from 43.52 µm to 602.3 µm, with a mean diameter of 209.7 ± 106.6 µm (Coefficient of Variation, $CV = 50.85\%$; $n = 915$) (Figure 1B, center; **Figure S2**, Supporting Information). Meanwhile, the GelMA microgels had a mean aspect ratio of 1.72 ± 0.51, and the aspect ratio also ranged broadly from 1.02 to 4.94. Producing heterogeneous structural microgels was an intentional choice in our system. Other methods have been used to make microgels with more uniform size and spherical shape, such as microfluidic devices ($CV < 3\%$) or batch emulsion ($CV \approx 10 - 25\%$).[5, 10, 18, 20] However, the heterogeneous shape of microgels produced using extrusion fragmentation has been proposed to promote microgel interdigitation, which increases the storage modulus of the jammed slurry compared to more uniform microgels.[37] In a 3D printing context, this can improve the printability of the ink. The coefficient of variation for the diameter of our GelMA microgels ($CV \approx 50\%$) is similar to that of other microgels produced using extrusion fragmentation ($CV \approx 25 - 50\%$).[37]

We chose to produce the sacrificial microgels from oxidized alginate (AlgOx), a degradable alginate derivative. The linear polysaccharide alginate has a long history as a cell-compatible biomaterial for cell encapsulation and culture.[39-41] Historically, however, alginate hydrogels have struggled with slow biodegradation. To address this, alginate can be oxidized with sodium periodate using a reaction first described by Malaprade in 1928.[40, 42-45] We employed this approach to produce AlgOx with a theoretical 5% degree of oxidation. Alginate oxidation and dialdehyde formation were confirmed using ^{1}H NMR (Figure S1, Supporting Information).[46] This degree of oxidation was chosen based on previous reports that it increases the degradation rate while preserving alginate's ability to ionically crosslink in the presence of divalent cations, such as calcium.[40] Ionic gelation offers a route towards cell-friendly, calcium-mediated microgel fabrication.[33, 47] Here we adapted a centrifugal microdroplet method to produce our sacrificial AlgOx microgels (Figure 1A, right).[47, 48] This process used a centrifuge-driven device to rapidly create microgels whose size was dictated by Tate's law. Briefly, upon centrifugation, pendant microdroplets of an AlgOx solution detach from the device nozzle when the centrifugal gravitational force (F_g) exerted on the droplet exceeds the counteracting force of surface tension (F_s). Once detached, the AlgOx microdroplets were captured and crosslinked within a calcium chloride ($CaCl_2$) reservoir. The size and shape of the AlgOx microgels could be controlled by several tunable variables, including centrifugal force, nozzle-to-calcium gap length, and calcium concentration (**Figure S3**, Supporting Information). Furthermore, sacrificial AlgOx microgel degradation was validated using varied buffer conditions (**Figure S4**, Supporting Information). While alginate oxidation is known to enable degradation through hydrolysis, we did not observe macroscopic evidence of microparticle degradation over 4 days when incubated in cell culture medium (Figure S4, Supporting Information).[40] To speed up the process of degradation, we dissociated ionic crosslinks within the alginate gel using the calcium chelators phosphate (in phosphate-buffered saline) or ethylenediaminetetraacetic acid (EDTA), both of which are known to degrade alginate gels (Figure S4, Supporting Information).[49-51] Optimized fabrication parameters produced relatively spherical AlgOx microgels with a mean diameter of 246.4 ± 33.3 μm ($CV = 13.51\%$, $n = 2285$) and a mean aspect ratio of 1.13 ± 0.12

(Figure 1B center, right). This diameter is within the range previously observed for microgels produced using a centrifugal approach; however, the variance in diameter seen in our AlgOx microgels is slightly greater than in previous reports ($CV \approx$ 1.5-10%).[47, 48] We hypothesize that this is due to smaller-diameter satellite microparticles included in our analyses, similar to those seen and excluded by others.[48] When we compared our structural GelMA and sacrificial AlgOx microgel populations, we observed that the mean diameters of the AlgOx microgels and the GelMA microgels were similar. However, the AlgOx microgels displayed lower variance in both diameter and aspect ratio than the intentionally heterogeneous GelMA microgels (Figure 1B, center). While other methods have been used to produce alginate-based microgels with reduced dispersity, including microfluidic devices and airflow-mediated droplet generation, these strategies require specialized equipment and extensive troubleshooting to maximize microgel reproducibility and cell viability.[33, 52-55] In contrast, the centrifugal microdroplet device utilized in this study can be created in one afternoon using standard laboratory consumables and tools available at most hardware stores.[47] The ease of setup and facile scalability of this centrifugal approach suited our need to rapidly create multi-milliliter-scale batches of jammed, cell-containing AlgOx microgels for 3D printing. Furthermore, while biopolymers such as gelatin have been used successfully as sacrificial materials, we chose to employ AlgOx in our system due to its compatibility with this rapid fabrication method.[18, 19, 56, 57]

After fabrication, each microgel population was collected for subsequent use. Prior to 3D printing, we prepared a jammed slurry of **(1)** structural GelMA microgels without cells and **(2)** sacrificial AlgOx microgels with encapsulated cells. We hypothesized that the ratio of GelMA to AlgOx microgels within the ink could be used to alter the total void fraction independent of ink printability (Figure 1C). Previous work demonstrated that blending multiple microgel types produces a well-mixed network of the two microgel populations.[15, 18] After printing, exposing the construct to UV light covalently crosslinks and anneals the GelMA microgels while leaving the AlgOx microgels unchanged (Figure 1D, left). The cell-containing, sacrificial AlgOx microgels rapidly degrade in culture to reveal void space and release cells throughout the depth of the construct (Figure 1D center, right).

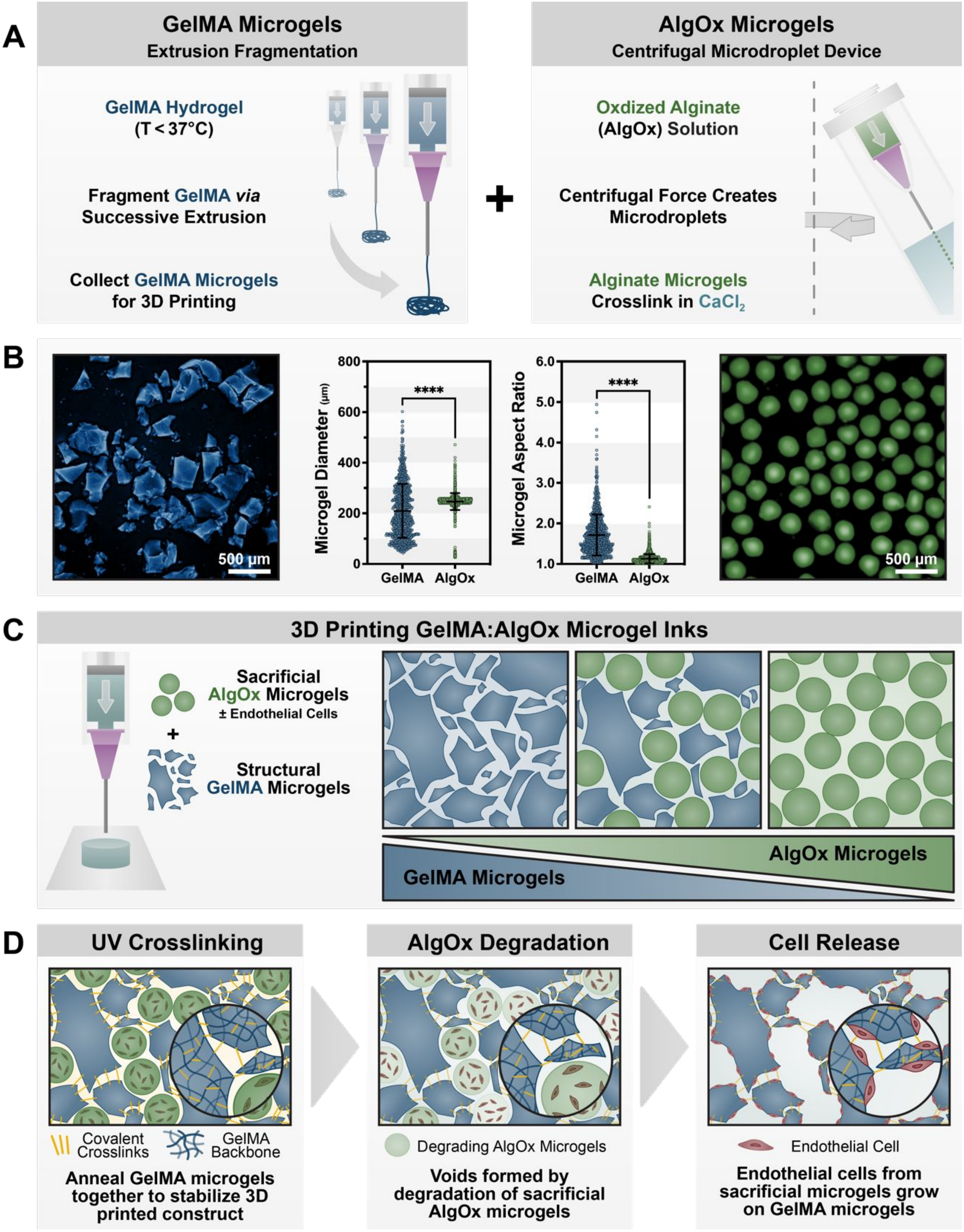

Figure 1. Design of granular inks composed of structural, UV-crosslinkable GelMA and sacrificial, cell-containing AlgOx microgels to enable direct cell printing and tunable void fraction. **(A)** Schematic depictions of microgel fabrication. GelMA microgels are fragmented from a hydrogel precursor by successively extruding through needles of decreasing size (left). Meanwhile, centrifugal force is used to extrude microdroplets of oxidized alginate (AlgOx) solution (with encapsulated cells) into a reservoir of calcium chloride ($CaCl_2$), where they ionically crosslink and form microgels (right). **(B)** False-colored representative images of resultant microgels are shown (left: GelMA, blue; right: AlgOx, green) beside quantification of their diameter and aspect ratio (center). Scale bars represent 500 µm. Data are plotted as mean ± standard deviation with a superimposed scatter plot of all points. Statistical significance was evaluated using an unpaired t test; $****p < 0.0001$. **(C)** The structural, UV-

crosslinkable GelMA and sacrificial, cell-containing AlgOx microgels are blended in different ratios to control the total void fraction within GelMA:AlgOx microgel inks. **(D)** GelMA microgels are annealed with UV crosslinking after 3D printing (left). Sacrificial AlgOx microgels rapidly degrade to reveal internal voids (center) and release encapsulated cells throughout the depth of the construct (right).

2.2. Extrudability and Stability of GelMA:AlgOx Microgel Inks

Ink extrudability is essential for extrusion-based 3D bioprinting, wherein inks must pass through a printing nozzle and form a cohesive, uniform filament. Inspired by recent work, we sought to assess eleven different GelMA:AlgOx microgel blends ranging from 100% structural GelMA microgels (100:0) to 100% sacrificial AlgOx microgels (0:100) for their extrudability and post-crosslinking stability.**[58]** The maximum hanging lengths of extruded filaments were used to evaluate the extrudability of each GelMA:AlgOx microgel ink composition (**Figure 2**A). Briefly, each GelMA and AlgOx microgel ink was loaded into a syringe fitted with a 20-gauge tapered dispensing nozzle (*ID* = 630 μm) and placed in the 3D printer. This nozzle size was determined empirically and is in accordance with previous reports demonstrating that polydisperse microgels require a nozzle approximately three times larger than the average particle diameter.**[58]** The entire sample was then slowly extruded (~ 1 mm s^{-1}), and the maximum hanging length before breakage was measured for all pendant samples (*n* > 15 per ink). For inks with low (or no) extrudability, the sample commonly resembled a pendant droplet that formed as the liquid phase of the ink was dispensed without successful rearrangement or flow of the constituent microgels.**[55, 58]** As extrudability increased, the microgel slurry yielded to initiate flow through the nozzle and filament formation. Meanwhile, the filament became more cohesive, increasing the hanging length.**[55, 58]** The mean hanging filament length for each ink is shown in Figure 2B. Additionally, the measured hanging filament lengths for selected GelMA:AlgOx inks with high, intermediate, and no GelMA content are shown in Figures 2C-E as a function of the percent volume extruded. Representative photographs of samples extruded at the beginning ('Begin') and the end ('End') of the test are also shown.

We observed that the ink made solely of sacrificial AlgOx microgels (0:100) only formed liquid droplets with a mean length of 4.1 ± 0.3 mm (Figure 2B). This ink showed no change in filament length throughout the test (Figure 2E), indicating the extrusion of the liquid phase and no yielding or flow of the AlgOx microgel-only slurry.**[55, 58]** Inspecting the compressed microgel plug after recovery from the syringe barrel confirmed these observations (**Figure S5**B, Supporting Information). The few microgels extruded with the liquid phase were deformed.

Based on these results, the 0:100 ink was deemed to be not extrudable. Similarly, inks 10:90 and 20:80 were not extrudable (data not shown).

Blending the sacrificial AlgOx microgels with at least 30% structural GelMA microgel content (30:70) rescued ink extrudability and produced filaments with a mean hanging length of 7.4 ± 5.6 mm (Figure 2B). Inks with intermediate blends of GelMA and AlgOx microgels, such as 50:50 and 60:40, also displayed intermediate extrudability, with mean hanging filament lengths of 7.2 ± 5.4 mm and 11.8 ± 10.3 mm, respectively (Figure 2B). Interestingly, these extrudable inks with intermediate blends (i.e., 50:50 and 60:40) exhibited striking heterogeneity in filament cohesion between samples formed at the beginning and end of the extruded volume (Figure 2D). Samples extruded at the beginning of the test ('Begin') formed pendant droplets or small filament fragments. As the test continued ('End'), the filaments became more cohesive, and the measured filament length increased. We hypothesize that this gradient of extrudability is due to further microgel jamming within the syringe, as reported with other granular inks.[58] At the beginning of the test, the microgels meet resistance in the nozzle, and the liquid phase surrounding them is extruded as droplets. With less fluid volume, the effective packing density increases until the applied force exceeds the resistance to extrusion, and the ink flows. While these extruded ink fractions (beginning and end) had qualitatively distinct viscoelastic properties, the reliable increase in filament length after extrusion of approximately 50 to 70% of the ink volume demonstrates that we can reproducibly achieve a printable jamming density using extrusion-mediated compaction. Therefore, we deemed inks with this gradient behavior to be extrudable. For subsequent experiments, we monitored ink properties and tested the extrudable, cohesive volume fraction.

Inks with the greatest proportion of structural GelMA microgels (90:10 and 100:0) had the highest and most consistent extrudability, with mean hanging filament lengths of 29.3 ± 4.1 mm and 30.0 ± 8.6 mm, respectively, and stable, cohesive filaments (Figure 2B). Furthermore, these inks showed high extrudability throughout the entire test, as demonstrated by longer filament lengths than other conditions (Figure 2C). Interestingly, the GelMA microgel-only ink (100:0) showed alternating filament lengths between approximately 24.8 mm and 45.8 mm for the first half of the extruded volume, with stabilization of filament length in the latter half of the test, akin to what is seen in intermediate blends (Figure 2D). Adding 10% AlgOx microgel content helped stabilize filament formation, and the 90:10 ink showed relatively consistent filament lengths between 22.6 mm and 36.2 mm. This investigation determined that the GelMA:AlgOx inks with ratios ranging from 100:0 to 30:70 were extrudable. Furthermore, we surmised that structural GelMA microgel content was the main driver of extrudability in our system.

We next assessed the mechanical stability of extrudable inks after sacrificial AlgOx microgel removal. For this test, cast disks of extruded GelMA:AlgOx inks were crosslinked by UV light and incubated in phosphate-buffered saline at 37 °C to facilitate AlgOx microgel degradation. Sample stability was assessed qualitatively by visual inspection and physical manipulation. This investigation showed that GelMA:AlgOx microgel inks with at least 50% structural GelMA microgel content (inks 100:0 through 50:50) were stable after sacrificial AlgOx microgel dissolution, while those with lower GelMA microgel content were not (Figure S5C, Supporting Information). The six extrudable and stable GelMA:AlgOx microgel blends were chosen for further rheological investigation: 100:0, 90:10, 80:20, 70:30, 60:40, and 50:50 (Figure S5D, Supporting Information).

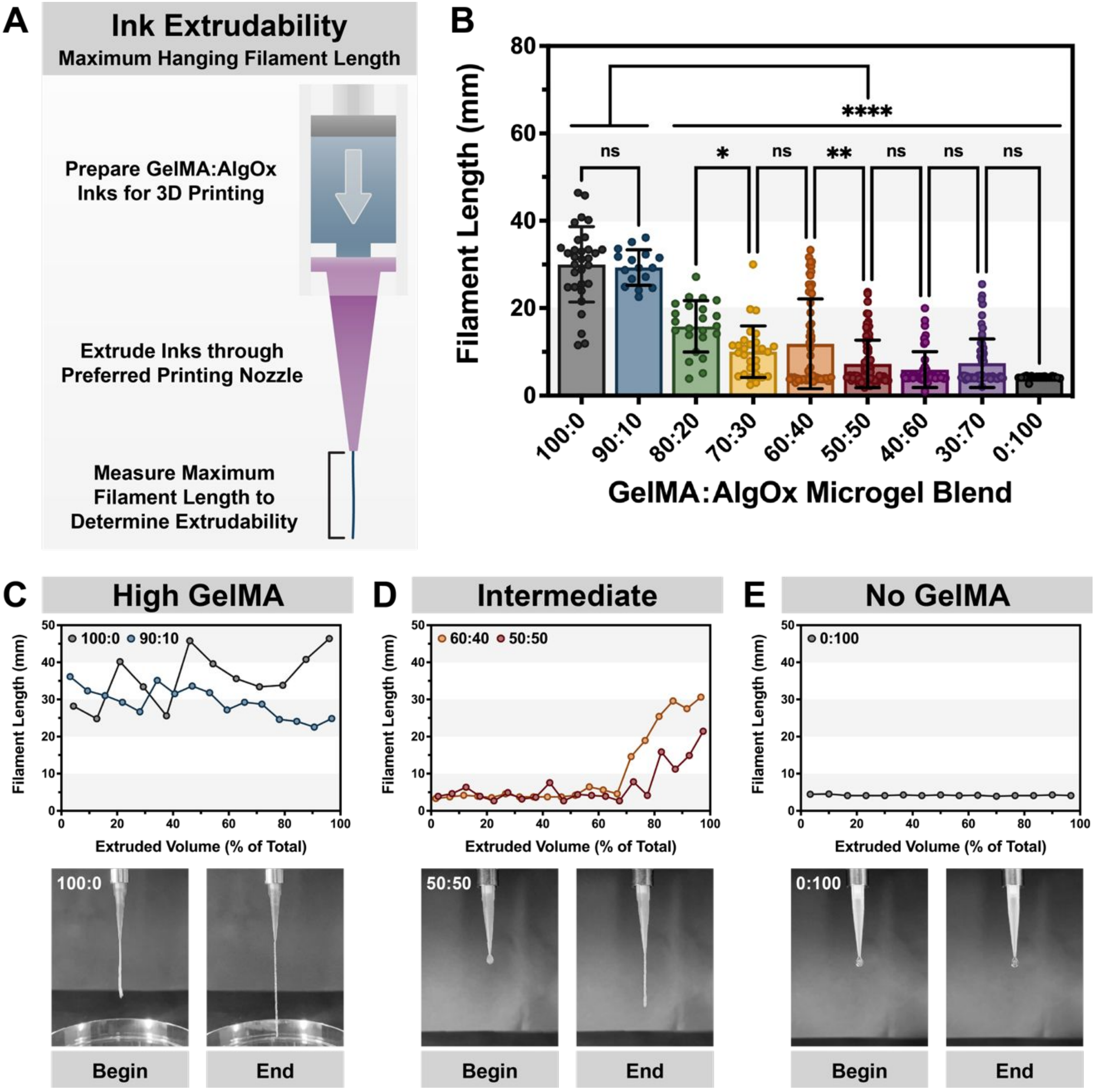

Figure 2. The extrudability of GelMA:AlgOx microgel inks. (A) GelMA:AlgOx ink extrudability was assessed by measuring the maximum hanging length of extruded filaments prior to breakage. Inks that were not extrudable formed shorter droplets, while extrudable inks formed longer, more cohesive filaments. **(B)** Quantified filament lengths for each GelMA:AlgOx ink formulation. Data are plotted as mean ± standard deviation, with a superimposed scatter plot of individual points. Statistical significance was evaluated using one-way ANOVA with Tukey's post hoc analysis; n.s. = not significant ($p > 0.05$), *$p < 0.05$, **$p < 0.01$, ***$p < 0.001$, ****$p < 0.0001$. **(C–E)** Representative data showing individual filament lengths measured as a function of the total volume extruded (top) and representative photographs of extruded samples at the beginning and end of the total volume (bottom) for selected inks with high (**C**, 100:0 and 90:10), intermediate (**D**, 60:40 and 50:50) and no (**E**, 0:100) GelMA microgel content.

2.3. Rheological Properties of Extrudable GelMA:AlgOx Microgel Inks

The viscoelastic properties of an ink combined with printing parameters are central to material performance. For extrusion-based 3D bioprinting, an ideal ink will display characteristics that aid the printing process, including cohesive filament formation, while limiting unfavorable ones, such as unwanted filament spreading.[7, 8] Each stage of 3D printing – before, during, and after – can be simulated using oscillatory shear rheology to provide insights into ink behavior. An exemplary biomaterial ink for extrusion-based bioprinting will exhibit solid-like properties in the printing cartridge (i.e., syringe), which traditionally prevents de-mixing during the printing process and improves printed shape fidelity.[7, 8] All six GelMA:AlgOx microgel inks exhibited a shear storage modulus (G') greater than the shear loss modulus (G'') within the linear viscoelastic region, confirming the elastic, solid-like properties of these jammed granular inks (**Figure 3**A). Inks with high structural GelMA microgel content that displayed the largest hanging filament lengths (100:0 and 90:10, Figure 2B) had the lowest storage moduli (483 ± 129 Pa and 454 ± 110 Pa for 100:0 and 90:10, respectively; Figure 3B). GelMA:AlgOx inks with a greater proportion of sacrificial AlgOx microgels, such as 80:20, 70:30, and 50:50, had higher storage moduli of 1151 ± 194 Pa, 897 ± 516 Pa, and 1405 ± 452 Pa, respectively. Unexpectedly, the 60:40 blend reproducibly had a storage modulus (496 ± 249 Pa) closer to those of the 100:0 and 90:10 blends despite behaving similarly to the 50:50 and 70:30 blends during extrudability testing (Figure 2).

In addition to storage modulus, the yielding behavior of the ink is important for determining the strain required to induce flow during printing.[7, 8] We investigated this behavior by monitoring the shear moduli of the GelMA:AlgOx microgel inks in response to increasing amounts of strain (Figure 3C). All six inks displayed a critical strain, after which the interparticle forces that confer solid-like behavior on the unannealed slurry began dissociating to allow material flow. We defined the critical strain as the strain at which the loss modulus became greater than the storage modulus (i.e., $G' > G''$).[59] Critical strain increased with sacrificial AlgOx microgel content, starting at ~32% for the 100:0 ink and increasing to ~67% for the 50:50 blend (Figure 3C). The relationship between microgel characteristics, such as stiffness and size, and emergent granular hydrogel properties is an area of active research.[55, 58, 59] Recent findings using single-microgel-type granular hydrogels composed of poly(ethylene glycol) (PEG) microgels showed that the G'/G'' crossover point occurs at larger strains for softer microgels and proposed microgel deformation as the cause. In that system, microgel size did not strongly affect critical strain.[59] Meanwhile, additional research with PEG microgels saw an increase in yield stress with stiffer, less deformable microgels, similar to the trends herein where critical strain increased with AlgOx microgel content.[58] As granular hydrogels see greater use in the biomaterials and bioprinting communities, continued experimental and theoretical investigation into the relationship between microgel properties and the emergent macroscale behavior of granular hydrogels becomes even more pressing.[60] Specifically, similar studies that use granular hydrogels composed of multiple types of microgels, such as these two-component GelMA:AlgOx inks, remain an area for future research.

Viscosity is another major determinant of ink printability. For example, during printing, the ink's viscosity must decrease to an extent that allows flow while still promoting filament formation. Upon deposition, the ink must regain its initial viscosity. This recovery helps the ink resist unwanted material deformation and improves shape fidelity.[7, 8] Figure 3D shows the measured viscosity of each GelMA:AlgOx microgel ink as a function of shear rate. Previous work with GelMA microgel-based inks identified that a minimum low shear viscosity of 100 Pa·s was necessary to achieve high shape fidelity after printing.[18] All six GelMA:AlgOx microgel inks have a low-shear viscosity between 1,500 and 4,500 Pa·s (shear rate ~ 0.02 s^{-1}), well above this 100 Pa·s minimum (Figure 3D). Moreover, all inks display shear-thinning behavior as indicated by a decreasing viscosity with an increasing shear rate.

While the ability to flow is essential for enabling material extrusion, ink behavior after deposition is equally fundamental in determining its utility for 3D bioprinting. In particular, material self-healing, or the time-dependent recovery of pre-extrusion viscoelastic properties, promotes high shape fidelity.[7, 8] To characterize this healing behavior, we subjected representative inks with high (100:0 and 90:10, Figure 3E) and intermediate (60:40 and 50:50, Figure 3F) structural GelMA microgel content to alternating periods of high and low shear stress. The shear moduli of each ink were monitored across a broad range of shear stress to select high and low shear stress values above and below the G'/G'' crossover point, respectively (**Figure S6**, Supporting Information). When experiencing low shear stress, such as in the syringe before printing, each ink demonstrates solid-like elastic behavior with a storage modulus greater than the loss modulus ($G' > G''$), as seen in Figure 3A. When higher shear stress is applied, similar to extrusion through a nozzle, the inks quickly adopt a liquid-like viscous state ($G'' > G'$). This further corroborates the shear-thinning behavior demonstrated through viscosity measurements (Figure 3D). Once shear stress is reduced, much like after filament deposition, the inks rapidly recover a solid-like, elastic state with storage and loss moduli similar to those seen before shearing. These rheological analyses demonstrate that our family of six extrudable and stable GelMA:AlgOx microgel inks all display the viscoelastic characteristics desirable for extrusion-based 3D bioprinting. Therefore, we subsequently assessed printed shape fidelity using these six microgel inks.

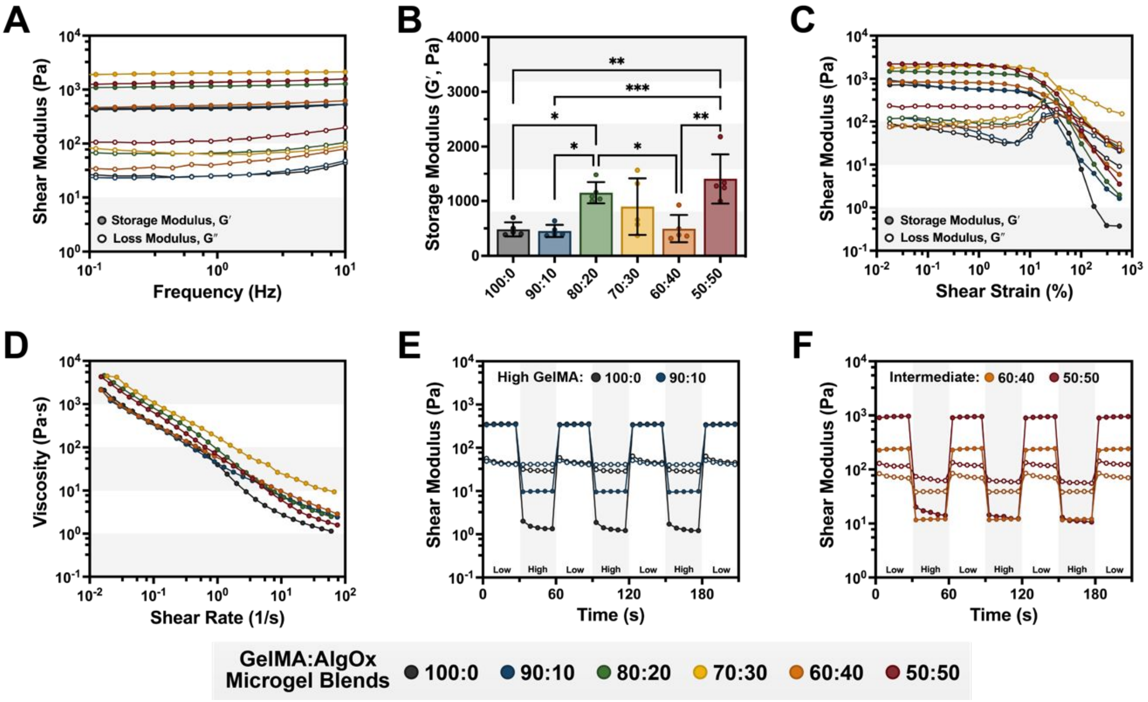

Figure 3. The viscoelastic properties of GelMA:AlgOx microgel inks. (A) Shear moduli of GelMA:AlgOx microgel inks as a function of oscillation frequency (0.1–10 Hz, 1% strain) demonstrating that all inks display a linear viscoelastic region with storage moduli (*G*′, filled symbols) greater than loss moduli (*G*″, open symbols). **(B)** Storage moduli of GelMA:AlgOx microgel inks (1 Hz, 1% strain). Data are plotted as mean ± standard deviation. Statistical significance was evaluated using one-way ANOVA with Tukey's post hoc analysis; n.s. = not significant ($p > 0.05$), *$p < 0.05$, **$p < 0.01$, ***$p < 0.001$, ****$p < 0.0001$. **(C)** Storage moduli (*G*′, filled symbols) and loss moduli (*G*″, open symbols) of GelMA:AlgOx microgel inks as a function of shear strain (0.01–1000% strain, 1 Hz). **(D)** Shear viscosity with increasing shear rates (0.01–100 s^{-1}) of GelMA:AlgOx microgel inks. **(E, F)** Shear-thinning and self-healing behavior of selected GelMA:AlgOx microgel inks with high GelMA microgel content (100:0 and 90:10, **E**) and intermediate GelMA microgel content (60:40, 50:50, **F**) under alternating low and high shear stress. Storage moduli (*G*′) are filled symbols, and loss moduli (*G*″) are open symbols.

2.4. Shape Fidelity When 3D Printing GelMA:AlgOx Microgel Inks

We evaluated the accuracy of a test shape printed from each GelMA:AlgOx microgel ink. This print accuracy, or ‘shape fidelity,' refers to the degree of similarity between a printed sample (‘3D Printing’) and its theoretical model (‘Design’) (**Figure 4**A). For this investigation, six GelMA:AlgOx microgel inks (100:0 through 50:50) were used to print a 2-layer, 15 mm by 15 mm lattice containing 36 square, open windows. Lattices such as this are commonly used to evaluate shape fidelity because their geometry readily allows for both qualitative and quantitative assessment.[8, 18, 61, 62] Here, shape fidelity was first qualitatively evaluated through visual inspection (Figure 4A). Successive lattice samples printed from the same preparation of intermediate blend inks, such as 60:40 and 50:50, displayed improved fidelity over time (**Figure S7**, Supporting Information). These intermediate blend inks formed increasingly cohesive filaments throughout printing, likely due to liquid exclusion and an effective increase in particle packing density. Samples printed with the initial ‘unjammed’ fraction failed to maintain open windows. Lattice morphology improved throughout printing, similar to the improvement in filament formation (as measured by hanging filament length) seen prior (Figure 2). Once sufficiently jammed, all six GelMA:AlgOx microgel inks allowed consistent extrusion, except for minor air inclusions resulting from the ink preparation process (Figure 4B, 80:20). Furthermore, lattices printed from all inks – 100:0 through 50:50 – visually showed comparable shape fidelity with open windows and similarly-sized filaments. Representative lattices printed from the compacted volume fraction are shown in Figure 4B. GelMA:AlgOx inks containing fluorescent AlgOx microgels were used to qualitatively investigate the distribution of sacrificial microgels within printed constructs (Figure 4C). Nonspecific light scattering outlined lattices printed using all inks, including the AlgOx microgel-free, non-fluorescent blend, 100:0. Close inspection of the 100:0 lattice confirmed the expected absence of fluorescent AlgOx microgels within printed filaments (Figure 4C, bottom left). In contrast, the 50:50 blend showed a strong signal within printed filaments due to the presence of fluorescent AlgOx microgels (Figure 4C, bottom right). These observations are confirmed through analysis of fluorescence intensity across four vertical struts and three corresponding lattice windows (Figure 4C, bottom center). Visual inspection of lattices printed from all inks demonstrated that the overall fluorescence increased in accordance with the proportion of AlgOx microgels within the ink blend. Furthermore, the distribution of AlgOx microgels was relatively uniform throughout each lattice. From this, we surmised that extrusion-mediated compaction did not affect the prepared GelMA:AlgOx microgel ratio and that all six GelMA:AlgOx inks had qualitatively similar lattice shape fidelity.

Next, we sought to quantitatively validate that the ratio of structural GelMA to sacrificial AlgOx microgels did not adversely affect ink printability. The open windows formed within the lattice were used to quantify metrics of shape fidelity, as previously described(Figure 4D).[18, 63, 64] These measurements compare the shape of printed windows to the theoretical ideal to highlight unfavorable ink behavior, such as unwanted spreading. A perfect lattice would contain square windows with an actual window area (A_a) equal to the theoretical window area (A_t). In practice, however, the actual area often differs from the theoretical area. For example, weak inks with poor filament formation or slow self-healing experience unwanted material flow or spreading after deposition, making A_a smaller than A_t. We define this ink spreading (Sp) as the percent difference between the actual and theoretical window area (Figure 4E; see **Equation 2** in the Experimental Section). A perfect window with $A_a = A_t$ would have an Sp of 0%, while a collapsed window with $A_a = 0$ would have an Sp of 100%. Representative lattices printed using the extrudable ink fraction were quantified and compared to lattices printed with the unjammed fraction. The mean Sp for most GelMA:AlgOx inks were similar, between 19% and 26%, regardless of AlgOx microgel content (Figure 4E). The 60:40 microgel blend experienced less ink spreading, evidenced by a lower mean Sp of ~8%. We supplemented these findings by exploring the shape of lattice windows through quantification of window printability (Pr_W).[18, 62, 63] This parameter uses a ratio between the window perimeter (P) and the window area (A_a) to determine how close the window is to a perfect square, similar to the roundness metric used to define circular objects (Figure 4F; see **Equation 3** in Experimental Section). A perfect, square window will have a Pr_W equal to 1. In reality, even inks demonstrating excellent filament formation can experience deformation at filament intersections due to gravity, resulting in a rounded square shape. In this case, Pr_W would be less than 1, or 0 for completely collapsed windows (when $Sp = 100\%$). Meanwhile, for inks with a microstructure that imparts filament topography, such as these GelMA:AlgOx granular inks, the actual perimeter may be larger than the theoretical window perimeter, making Pr_W greater than 1. As expected, the windows of 'unjammed' samples had a $Pr_W = 0$. Intact windows printed with the jammed fraction of all GelMA:AlgOx microgel inks showed similar values of Pr_W between 0.97 and 1.12, independent of the sacrificial AlgOx microgel content (Figure 4F). All inks were printed using the same parameters during this test, irrespective of ink viscoelastic properties. If higher accuracy was desired for printing application-specific 3D structures, the slight deformation in window shape and size with these inks could be improved further by adjusting these printing parameters, such as layer height, extrusion rate, or printing speed.[8, 61, 63, 64]

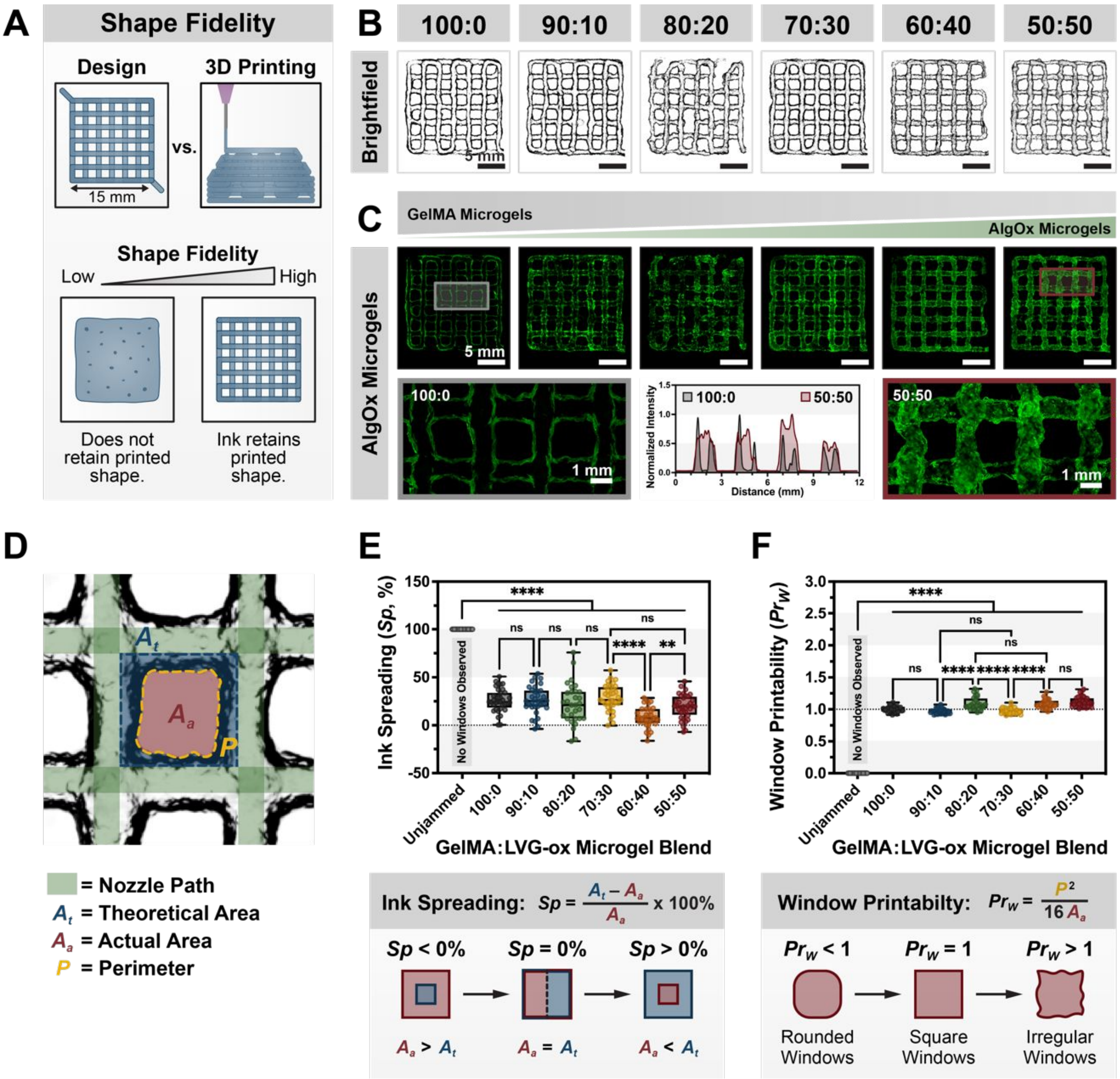

Figure 4. Shape fidelity of lattice structures printed using GelMA:AlgOx microgel inks. (A) Shape fidelity is characterized by printing a 15 mm by 15 mm lattice and comparing the printed sample to its 3D model. **(B)** Representative brightfield microscopic images of lattice structures 3D printed from GelMA:AlgOx microgel inks 100:0 through 50:50. Scale bars represent 5 mm. **(C)** Representative fluorescence microscopic images (top row) show the deposition of AlgOx microgels containing 2,000-kDa fluorescein isothiocyanate (FITC)-dextran within printed lattices. Insets show the absence of fluorescent microgels in the 100:0 filaments (bottom left) and the presence of AlgOx microgels within filaments of the 50:50 lattice (bottom right), confirmed by quantification of fluorescence intensity across the image (bottom center). Scale bars represent 5 mm (top row) and 1mm (bottom row). **(D)** Brightfield images were used to quantify metrics of shape fidelity based on the shape of the open windows formed within a printed lattice. **(E, F)** Quantified ink spreading (*Sp*, **E**) and window printability (Pr_W, **F**) of GelMA:AlgOx microgel inks. Data are plotted as a box and whisker plot, with whiskers showing the minimum and maximum values and a superimposed scatter plot of all points ($n \geq 30$ for all inks). Statistical significance tested by one-way ANOVA with Tukey's post hoc analysis; n.s. = not significant ($p > 0.05$), *$p < 0.05$, **$p < 0.01$, ***$p < 0.001$, ****$p < 0.0001$.

2.5. Void Fraction within GelMA:AlgOx Microgel Inks

Having established that GelMA:AlgOx microgel blends with at least 50% structural GelMA microgel content demonstrated the necessary characteristics of a printable ink, we next sought to investigate our hypothesis that sacrificial AlgOx microgel incorporation produces controllable void space within 3D printed samples. To that end, each GelMA:AlgOx microgel ink was prepared and used to print disks. Printed samples were crosslinked using UV light and incubated in a high molecular weight, fluorescein-labeled dextran solution containing a calcium chelator at 37 °C to dissociate the ionically crosslinked sacrificial AlgOx microgels. Dissociation of the sacrificial AlgOx microgels weakened the mechanical properties of the overall construct as expected, though the printed disks remained solid-like with a storage modulus higher than the loss modulus (**Figure S8**, Supporting Information). As the AlgOx microgels degraded, the fluorescent dye freely permeated throughout the open pores but did not enter the covalently crosslinked GelMA microgels. The pores were directly visualized using confocal microscopy and quantified to provide a measure of the total internal void fraction (**Figure 5**A). In the absence of sacrificial AlgOx microgels (i.e., the GelMA microgel-only, 100:0 blend), the voids within the construct were relatively small and irregular in shape (Figure 5B), and the total void fraction was 0.03 ± 0.02 (Figure 5C). This void morphology was expected for microgels with jagged shapes, such as our GelMA microgels (Figure S2, Supporting Information). Previous work has compared the characteristics of granular hydrogels composed of microgels produced using different methods, including microfluidic device and extrusion fragmentation. While the total void space within the granular hydrogels was relatively similar across all conditions (< 0.1), microgels made via extrusion fragmentation produced significantly more pores of smaller size.[37] For these GelMA:AlgOx inks, introducing just 10% sacrificial AlgOx microgel content (90:10) produced noticeably larger and more circular pores within the crosslinked samples and increased the total void fraction to 0.13 ± 0.04. The difference in internal void structure was striking upon the addition of at least 30% AlgOx microgel content. Interconnected chains of circular pores left by sacrificial AlgOx microgel dissolution were present in the 70:30, 60:40, and 50:50 inks. This also led to an increase in void fraction; the 70:30, 60:40, and 50:50 inks produced internal void fractions of 0.29 ± 0.07, 0.35 ± 0.07, and 0.33 ± 0.07, respectively. The higher void fractions observed within our GelMA:AlgOx inks were similar to the theoretical maximum achievable through particle packing: 0.36 for random close packing of monodisperse spheres.[65] Meanwhile, the range of void fractions produced by our family of GelMA:AlgOx inks was comparable to the individual void fractions seen in other granular hydrogels, reportedly between 0.1 and 0.33.[26, 28, 38, 66] The void fraction within these single-component granular hydrogels depends on microgel morphology and day-to-day variations in hydrogel preparation, making it challenging to control.[28] Modular inks like this GelMA:AlgOx system that uses sacrificial microgels to introduce porosity do not face this challenge. Previous studies have reproducibly achieved void fractions of up to 0.57 using sacrificial microgels.[18] We hypothesize that the irregular size and shape of the structural GelMA microgels paired with the more uniform geometry of the sacrificial AlgOx microgels facilitates the production of multiscale porosity within the construct. Observing 3D reconstructions of void space beside 2D image slices reveals that the GelMA microgels alone produce long, narrow interparticle voids on the order of tens of micrometers in diameter (**Figure S9A**, Supporting Information), ideal for capillary-mimetic endothelial cell sprouting.[2] Meanwhile, the percolating network of sacrificial, cell-containing AlgOx microgels produces a tunnel of large-diameter interconnected pores within which the released cells can grow.[2] The heterogeneity in microgel morphology used in this system allows for multiscale complexity within the ink microarchitecture. These differences in both the dimensions and geometry of pre-formed voids could be leveraged in the future to modulate cell behaviors, including proliferation and migration.[10, 17, 24] Through quantifying the void fraction, we validated that the introduction of sacrificial AlgOx microgels predictably produces increased porosity within the 3D printed and crosslinked GelMA:AlgOx inks.

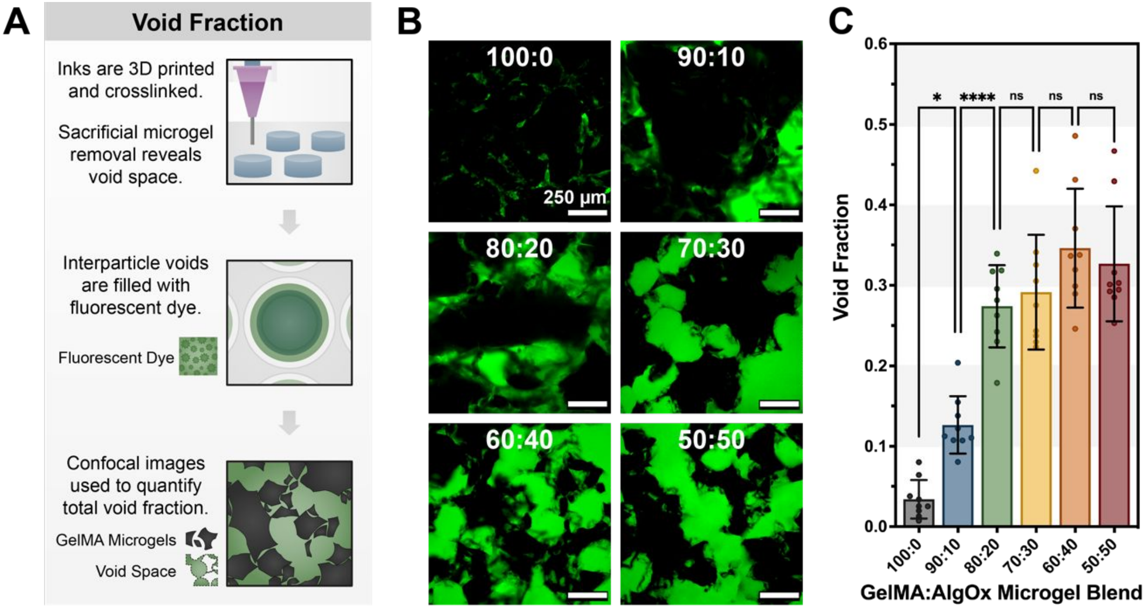

Figure 5. The void fraction within 3D printed GelMA:AlgOx microgel inks after UV crosslinking and sacrificial AlgOx microgel removal. (A) After 3D printing and UV crosslinking disks made from each GelMA:AlgOx ink, the samples were incubated in phosphate-buffered saline containing 2,000-kDa FITC-dextran and the calcium chelator ethylenediaminetetraacetic acid (EDTA). As the AlgOx microgels dissociated, the large molecular weight dextran permeated throughout the revealed void space but remained excluded from covalently crosslinked GelMA microgels. This enabled the visualization and quantification of the internal void fraction. **(B)** Representative images of void space within GelMA:AlgOx inks. GelMA microgels are shown in black, and the void space is shown in green. Scale bars represent 250 µm. **(C)** Quantified void fraction within GelMA:AlgOx inks with microgel ratios ranging from 100:0 to 50:50. Data are plotted as mean ± standard deviation, with a superimposed scatter plot of all points. Statistical significance tested by one-way ANOVA with Tukey's post hoc analysis; n.s. = not significant ($p > 0.05$), *$p < 0.05$, **$p < 0.01$, ***$p < 0.001$, ****$p < 0.0001$.

2.6. GelMA:AlgOx Microgel Inks Enable Depth-Independent Deposition of Encapsulated HUVEC

Finally, we used the GelMA:AlgOx blends as bioinks to examine whether encapsulation of cells within the sacrificial microgels allowed the generation of 3D bioprinted samples with uniform cell distribution throughout the depth of the construct. One primary advantage of this two-component granular ink is the opportunity to encapsulate and directly print cells within the sacrificial AlgOx microgels to accelerate the introduction of cells within a printed construct. In our work, HUVEC were readily encapsulated within sacrificial AlgOx microgels fabricated using a centrifugal microdroplet device. The addition of cells had a negligible effect on the diameter of the sacrificial AlgOx microgels (**Figure S10**, Supporting Information). Acellular AlgOx microgels had a mean diameter of 246.4 ± 33.3 μm (CV = 13.51%, n = 2285), while those containing HUVEC had a mean diameter of 248.9 ± 26.3 μm (CV = 10.56%, n = 1848). The aspect ratio was similarly unchanged, with mean values of 1.18 ± 0.15 and 1.13 ± 0.12 for AlgOx microgels with and without HUVEC, respectively. Moreover, HUVEC maintained high viability after encapsulation within calcium-crosslinked AlgOx microgels: 87% of HUVEC remained viable immediately after encapsulation compared to 95% before microgel fabrication (**Figure 6**A). Fluorescence microscopic images confirm the encapsulation of HUVEC within individual AlgOx microgels (Figure 6A). After fabrication, cell-containing, sacrificial AlgOx microgels were collected and blended with structural GelMA microgels to form three GelMA:AlgOx bioinks with varying sacrificial AlgOx microgel content: 90:10, 60:40, and 50:50. These ink formulations were chosen because they covered a range of low (90:10) and high (60:40 and 50:50) void fraction (0.13 ± 0.04 to 0.35 ± 0.07, Figure 5) and cell dosing. These GelMA:AlgOx bioinks were used to 3D bioprint disks (8 mm x 1 mm) that were subsequently crosslinked with UV light, washed thrice with Dulbecco's phosphate-buffered saline (DPBS) to accelerate AlgOx dissociation, and cultured for up to seven days. During that time, the AlgOx microgels degraded to release encapsulated HUVEC, which then grew along the surface of interparticle voids. Although EDTA rapidly (~ 1 min; Figure S4, Supporting Information) degrades the AlgOx microgels, its cytotoxicity prevents its use in the presence of cells (post-EDTA viability of ~36%; **Figure S11**, Supporting Information). Instead, treatment with phosphate-buffered saline proved a cell-friendly method for accelerating the dissociation of AlgOx microgels (post-DPBS viability ~85%; Figure S11, Supporting Information). We relied upon a combination of hydrolytic degradation of oxidized alginate and gentle calcium complexation to release encapsulated cells. The rate and timing of this degradation could be controlled in the future by altering the degree of oxidation and alginate concentration, or through the temporary addition of calcium chelators to trigger the disruption of ionic crosslinks.[40, 44, 67] This controllable cell release would not be possible in a single-component granular ink. Using two microgel components allows us to decouple structural integrity, maintained by covalently crosslinked GelMA microgels, and cell release, enabled by sacrificial AlgOx microgel dissolution. Moreover, the quantity and interconnectivity of voids, such as those introduced by AlgOx microgel degradation (Figure 5), have been shown to positively affect cell viability, migration, and morphology.[16-19] In our system, HUVEC grown within GelMA:AlgOx disks showed visually distinct morphologies after seven days in culture that correlated with void fraction (Figure 6B). Immediately after encapsulation, when cells are entrapped within AlgOx microgels, the cells appear rounded. Similarly, cells cultured within the low void fraction, 90:10 ink for seven days (void fraction of 0.13 ± 0.04) remained compact. Meanwhile, those grown in the 60:40 and 50:50 inks containing more void space (void fractions of 0.35 ± 0.07 and 0.33 ± 0.07, respectively) showed greater spreading along the surface of structural GelMA microgels, as evidenced by larger average cell volumes (Figure 6C). While the 60:40 and 50:50 inks had similar void fractions, we saw more cell spreading in the 50:50 ink. We hypothesize this may be due to the greater number of cells present in the higher AlgOx content 50:50 constructs, which may lead to increased opportunities for cell-cell contacts and local paracrine secretion that promote cell spreading.[18, 68, 69] We further compared HUVEC response to either encapsulation within AlgOx microgels or blending throughout interparticle voids prior to 3D bioprinting (**Figure S12**, supporting information). Data demonstrate that cells in both conditions showed similar viability after one day in culture; however, cells encapsulated within AlgOx microgels demonstrated greater spreading over time, likely due to an effective local increase in cell density that again provides greater opportunity for cell-cell contacts and paracrine signaling known to be important for endothelial cell health.[18, 68, 69]

After establishing that HUVEC grew within the selected GelMA:AlgOx bioinks, we sought to confirm our hypothesis that printing cell-containing microgels would produce a uniform cell distribution throughout the depth of a 3D printed construct. To this end, confocal microscopy was utilized to obtain representative vertical image stacks (height ≥ 200 µm; z_0 = sample surface) of HUVEC within 3D printed disks. The resulting 3D image stacks were used to quantify cell distribution along the z-axis of the sample (Figure 6D). The mean cell location (i.e., cell depth) within 3D printed samples, measured by nuclear position, was similar across all three GelMA:AlgOx bioinks, with a slight increase in the 90:10 formulation (**Figure S13**, Supporting Information). However, the range in nuclear location was consistent in all three conditions. Normalizing the nuclear position to the maximum depth (~ 200 μm) and converting the data to a cumulative frequency distribution demonstrated that the vertical distribution of cell nuclei is similar for all three GelMA:AlgOx bioinks (Figure 6E). What is more, all three bioink formulations produced a distribution similar to the theoretical ideal (the line $Y = X$). When each data set was fit to a trendline, we saw that all trendlines had slopes close to the idealized model (i.e., ideal slope = 1; trendline slopes: 0.97 – 1.08), small intercepts (ideal intercept = 0; trendline intercepts: -0.05 – 0.06), and R-square values ~ 0.99 (Figure 6E). Representative images for each bioink are shown in Figure 6E, with the actin cytoskeleton displayed in white and nuclei false-colored to denote the z-position within the 200-μm-thick image stack (color map shown in Figure 6B). These results contrast sharply with our previous work that leveraged tunable void fraction to promote endothelial cell infiltration from the sample surface (Figure 6F).[18] After seven days of culture, we previously saw that cells seeded on the surface of inks with a void fraction of 0.20, comparable to the void fraction of these GelMA:AlgOx microgel inks, migrated a mean distance of only 11.55 ± 5.03 μm into the construct (Figure S13, Supporting Information). While increasing the void fraction to 0.57 significantly enhanced cell migration, the cell distribution remained skewed toward the construct surface. Few cells were observed near depths of 200 μm, and the mean nuclear position was 69.84 ± 41.36 μm (Figure 6F). In contrast, in our GelMA:AlgOx system, the mean cell positions were 107.8 ± 54.4 μm, 97.2 ± 61.9 μm, and 95.8 ± 54.3 μm for the 90:10, 60:40, and 50:50 inks, respectively, with a uniform cell distribution across a 200 μm vertical section (Figure 6E).

As granular inks see increased use, we anticipate the 3D bioprinting community will begin to create biomaterial inks with greater functionality and complexity, such as this family of two-component granular inks. For example, recent works have leveraged physical microgel characteristics, such as aspect ratio, to improve the injectability and porosity of granular hydrogels.[25-27] Altering microgel geometry in this way remains an interesting area for future exploration, particularly in the context of modular, multi-component inks. Furthermore, the bioactivity of granular inks could be expanded in a number of ways. The adhesion and proliferation of released cells could be optimized by adding cell type-specific adhesive ligands to the structural microgels within the construct. Moreover, the biomimicry of granular inks could be expanded by producing cell-laden microgels containing various tissue-specific cell types. Alternatively, cells could be introduced within granular inks using multiple methods, such as within sacrificial microgels and inside interparticle pores. Sacrificial microgels with tunable degradation rates could further be employed for the timed release of soluble cell-instructive signals, such as angiogenic growth factors.[70] These opportunities highlight that modular, two-component granular inks such as this GelMA:AlgOx microgel ink allow the use of myriad biopolymers for either the structural or sacrificial component and are therefore widely adaptable to numerous applications. What is more, these exciting opportunities illustrate the vast potential of granular inks for solving current challenges in 3D bioprinting.

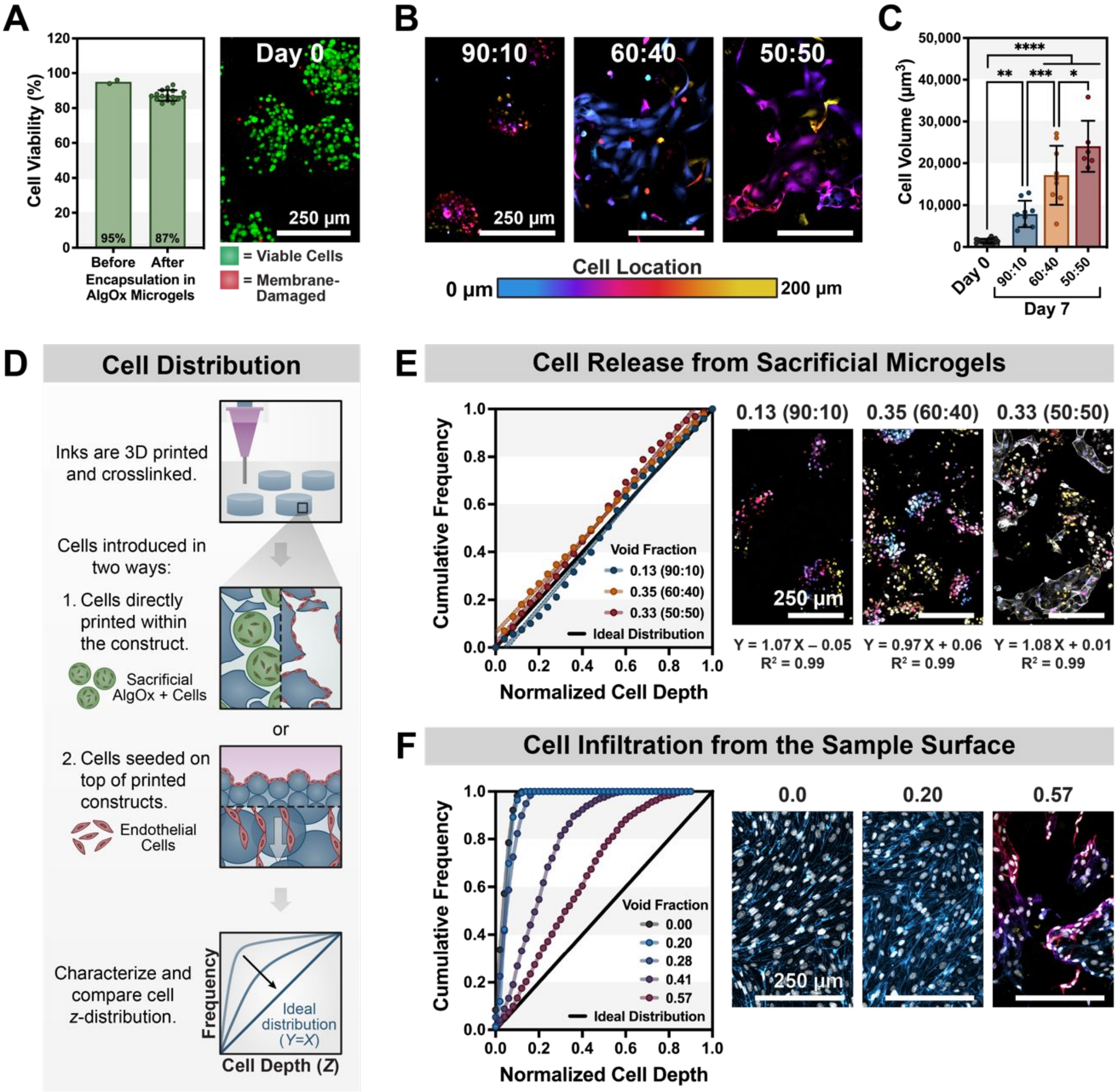

Figure 6. Sacrificial, cell-encapsulating microgel-based bioinks enable 3D printing of constructs with homogenous cell distributions throughout the sample. (A) Human umbilical vein endothelial cells (HUVEC) maintain high viability after centrifuge-driven fabrication of cell-containing AlgOx microgels. Data are plotted as mean ± standard deviation, with a superimposed scatter plot of all points. Representative image of HUVEC-laden AlgOx microgels stained with Live/Dead™ immediately after fabrication (green: viable cells; red: membrane-damaged cells). **(B)** HUVEC 3D printed and cultured within 90:10, 60:40, and 50:50 bioinks for seven days show visually distinct morphological differences, with greater cell spreading in bioinks with higher porosity. Cells were stained with Calcein AM and false-colored according to z-position within a 200 μm image stack. **(C)** The volume (μm³) of cells cultured for seven days within GelMA:AlgOx microgel inks compared to samples imaged immediately following encapsulation confirm visual trends. Data are plotted as mean ± standard deviation, with a superimposed scatter plot of all points. Statistical significance tested by one-way ANOVA with Tukey's post hoc analysis; n.s. = not significant ($p > 0.05$), *$p < 0.05$, **$p < 0.01$, ***$p < 0.001$, ****$p < 0.0001$. **(D)** In order to quantify cell distribution, cell-containing AlgOx microgels are blended with GelMA microgels to prepare cell-laden bioinks. The bioinks were then printed, UV-crosslinked, and cultured. After seven days, the samples were imaged using confocal microscopy to assess the vertical distribution of cells throughout the depth of the construct, and compared to samples that rely upon cell infiltration from the sample surface. When cellular *z*-position is plotted

as cumulative frequency, an ideal, uniform distribution would produce the linear trendline $Y = X$. **(E)** The normalized *z*-position of cell nuclei within a 200-µm-thick image stack demonstrated that direct deposition of cell-laden microgels leads to homogenous cell distributions. Data are plotted as a cumulative frequency distribution (circles) with a corresponding trendline and 95% confidence interval (filled areas between fine dashed lines) (left). Representative images of HUVEC cultured within 3D printed disks, with the trendline and *R*-square value listed (right). Nuclei are false-colored to represent the *z*-position within the printed ink (blue: 0 µm; yellow: 200 µm; colormap shown in C). The actin cytoskeleton is false-colored white. **(F)** In contrast, the normalized *z*-position of cell nuclei within the sample relying upon void fraction-mediated cell infiltration demonstrated a distribution of nuclei skewed toward the sample surface, even in samples with high void fractions. Data are plotted as a cumulative frequency distribution (circles) with a connecting line (left). Representative images of HUVEC that infiltrated into 3D printed disks (right). Nuclei are false-colored white. The actin cytoskeleton is false-colored to represent the z-position within the printed ink (colormap shown in C). Scale bars in A, B, E, and F represent 250 µm.

3. Conclusion

Microgel-based granular inks have a unique ability to satisfy the viscoelastic requirements of extrusion-based 3D bioprinting while providing cell-instructive cues, such as microporosity. Yet these inks often rely upon void fraction-mediated infiltration to introduce cells within printed constructs, which requires significant time due to their slow migration. This work uses a two-component granular ink composed of structural, UV-crosslinkable GelMA microgels and sacrificial, cell-laden AlgOx microgels to produce a uniform cell distribution within the ink, independent of void fraction. Inks with up to 50% sacrificial AlgOx microgel content (blends 100:0 through 50:50) display desired viscoelastic properties and high shape fidelity. Altering the ratio of structural GelMA to sacrificial AlgOx microgels produced a family of GelMA:AlgOx microgel inks that could be used to 3D print constructs with multiscale porosity and a total void fraction ranging from 0.03 ± 0.02 to 0.35 ± 0.07 (for 100:0 and 60:40, respectively). In vitro studies demonstrated the suitability of these inks for endothelial cell culture. Cells maintained a high degree of viability after the centrifuge-mediated formation of cell-encapsulating, sacrificial AlgOx microgels and showed distinct morphological differences after seven days of culture in low and high void fraction inks. Finally, an investigation of cellular position confirmed that cell release from sacrificial AlgOx microgels produced an ideal cell distribution throughout the depth of printed samples independent of void fraction. Overall, this work presents a method for expanding the potential of granular inks by employing both microgel modularity and cell encapsulation to address the need for rapid cellularization of thick, 3D printed constructs for tissue engineering and regenerative medicine.

4. Experimental Section

***GelMA Synthesis*:** Gelatin methacryloyl (GelMA) was synthesized using a one-pot approach as previously described.[18, 35, 36] First, type A gelatin (300 bloom; Sigma-Aldrich) was dissolved at 20 wt% in 0.1 M carbonate-bicarbonate (CB) buffer (e.g., 3.18 g sodium carbonate and 5.86 g sodium bicarbonate in 1 L distilled water) at 37 °C overnight while stirring. Once dissolved, sodium hydroxide was used to adjust the pH to 9. Then 0.1 mL of methacrylic anhydride (MAA, 94%; Sigma-Aldrich) per gram of gelatin was added to the 20 wt% gelatin solution while stirring at 700 rpm. The reaction was allowed to proceed for 2 h at 50 °C, after which the reaction mixture was diluted 1:10 using warm CB buffer to quench the reaction. The reaction product was collected into dialysis tubing (MWCO = 3.5 kDa; Repligen Spectra/Por) and dialyzed against distilled water for 5 days at room temperature. The dialyzed GelMA was then collected, sterile filtered using a 0.22 μm vacuum-driven filter unit (Nalgene™ Rapid-Flow™), and lyophilized in preparation for use.

Alginate Oxidation**:** Oxidized alginate (AlgOx) was prepared based on previously described methods.**[33, 40, 71]** First, low viscosity high G-content alginate ($G/M \geq 1.5$; Pronova UP LVG Alginate) was dissolved at 1 wt% in distilled water overnight at 37 °C while stirring. The following day, sodium periodate ($NaIO_4$, 99.9%; Acros Organics) was added dropwise to the alginate to achieve a theoretical oxidation of 5% of the uronic acid residues. The reaction was covered to protect it from light and allowed to proceed for 17 h while stirring at 500 rpm. Once complete, a molar excess of ethylene glycol (≥ 99%; Fisher BioReagents) was added to quench the reaction. The reaction product was collected into dialysis tubing (MWCO = 3.5 kDa; Repligen Spectra/Por) and dialyzed against distilled water for 3 days at 4 °C, changing the dialysis water twice on the first day and once for an additional two days. The dialyzed AlgOx was then collected, sterile filtered using a 0.22 μm vacuum-driven filter unit (Nalgene™ Rapid-Flow™), and lyophilized in preparation for use.

Determination of Degree of Modification**:** The degree of substitution (GelMA) and oxidation (AlgOx) of each biopolymer was characterized using ^1H NMR. Lyophilized GelMA and gelatin type A were dissolved at 1 wt% in deuterium oxide (D_2O; Sigma-Aldrich). Integrals for relevant peaks were first normalized by the integral of the peak corresponding to aromatic tyrosine residues (7.25 ppm, peak a). Then, the degree of gelatin substitution (*DS*) was calculated using the ratio of integrals for the lysine-methylene peaks (3.02 ppm, peak d) of gelatin and GelMA.**[35, 72]** To determine the degree of alginate oxidation, AlgOx and unoxidized alginate were dissolved in D_2O containing 3-(trimethylsilyl)propionic-2,2,3,3-d_4 acid, sodium salt (TMS, 0.05 w/v %; Sigma-Aldrich) as an internal standard. While AlgOx was formed with a theoretical degree of oxidation (*DO*) of 5%, the actual *DO* was calculated using the ratio of the integrals for existing methyl protons (peak 3) to methyl protons formed through alginate oxidation (peaks 1 and 2).**[33]** The NMR spectra of samples were recorded on a Varian Unity INOVA 600 NMR spectrometer and analyzed with MNOVA software.

GelMA Microgel Fabrication via Extrusion Fragmentation**:** Extrusion fragmentation was used to fabricate GelMA microgels inspired by a previously reported protocol.**[37, 38]** GelMA stock solution was prepared at 15 wt% in Dulbecco's phosphate-buffered saline (DPBS) without magnesium and calcium (Corning) at 37 °C. Once fully dissolved, 1 mL of the 15 wt%

GelMA solution was added to a 3 mL syringe with the plunger removed. The plunger was then carefully reinserted, and the syringe was sealed and placed upright at 4 °C overnight to facilitate the thermal gelation of the precursor solution. A syringe pump (SyringeONE 1000 Series; New Era Instruments) was used to extrude the 15 wt% GelMA precursor gel and the resulting fragmented products through blunt end dispensing needles with decreasing inner diameter (*ID*): 18-gauge (*ID* = 965 µm), 23-gauge (*ID* = 355 µm), 27-gauge (*ID* = 210 µm), and 30-gauge (*ID* = 160 µm; Jensen Global). Between each step, up to 1 mL of cold DPBS per milliliter of precursor gel was added to aid extrusion and incorporated via stirring. Fragmented microgels were collected and stored on ice. After fragmentation was complete, GelMA microgels were resuspended in cold DPBS, centrifuged for 5 min at 5000 x *g* and 4 °C, and the supernatant was removed. A total of three washes were performed. Prior to use, washed GelMA microgels were incubated at 4 °C in DPBS containing 2.5 mM lithium phenyl-2,4,6-trimethylbenzoylphosphinate (LAP, ≥ 95%; Sigma-Aldrich) for at least 60 min to facilitate UV crosslinking.

To quantify the diameter and aspect ratio of GelMA microgels, dissociated samples were resuspended in a 1 mg mL^{-1} rhodamine B solution for 10 min. Stained GelMA microgel samples were imaged using a Leica THUNDER fluorescence microscope. FIJI was used to prepare representative images and quantify microgel morphology.[73] The diameter of individual microgels was calculated as the diameter of a circle with equivalent area. Microgel aspect ratio was calculated by dividing the major axis of the microgel (*b*) by its minor axis (*a*).

***AlgOx Microgel Fabrication via Centrifugal Microgel Device*:** A centrifugal microdroplet device inspired by previous reports was created using common laboratory consumables.[47, 48] The caps of 50 mL conical tubes were prepared by drilling a 10 mm opening through the center of the cap. Next, sharp forceps were used to carefully make two small (~2 mm) openings in 1.5 mL microcentrifuge tubes: (1) through the center of the lid and (2) through the center of the conical base. Then, a 30-gauge x 1-in dispensing nozzle (*ID* = 160 µm; Jensen Global NT Premium Series) was inserted into the 1.5 mL microcentrifuge tube, with the metal cannula fed through the hole in the tube's conical base. Nozzles were affixed within the microcentrifuge tubes using epoxy (2 Ton Epoxy; Devcon). Assembled devices were allowed to cure overnight.

For acellular microgel fabrication, an AlgOx precursor solution was prepared at 4 wt% in Hank's Balanced Salt Solution (HBSS) without calcium or magnesium (Gibco). The precursor was allowed to dissolve overnight at 37 °C while stirring. The following morning, AlgOx was diluted to a working concentration of 2 wt% using HBSS. Then, 1 mL of 2 wt% AlgOx in HBSS was added to each centrifugal microdroplet device. A 50 mL conical tube was filled with enough 50 mᴍ calcium chloride ($CaCl_2$) solution to achieve a nozzle-to-calcium gap length (L) of 2 mm between the end of the device nozzle and the $CaCl_2$ reservoir meniscus. Once assembled, the device was centrifuged for 30 s (for microgel characterization) or 2 min (for scaled production) at 500 x g to generate AlgOx microgels. The process was repeated as needed to create the desired volume of AlgOx microgel slurry. After fabrication, the microgels were allowed to crosslink and sediment via gravity for 15–30 min. The supernatant was then carefully removed to eliminate excess liquid, producing a granular slurry of AlgOx microgels ready for 3D printing.

To characterize the diameter and aspect ratio of AlgOx microgels, the 4 wt% AlgOx precursor solution was diluted 1:1 with HBSS containing 2 mg mL^{-1} fluorescein isothiocyanate-labeled dextran (FITC-dextran, molecular weight = 2,000 kDa; Sigma-Aldrich). AlgOx microgels were then fabricated using the centrifugal microdroplet device, as described above. Several fabrication parameters, including nozzle-to-calcium gap length (L), centrifugal force, and $CaCl_2$ concentration, were tested to determine their effect on AlgOx microgel size and shape (see Figure S3, Supporting Information for a list of tested parameters). AlgOx microgels containing FITC-dextran were imaged using a Leica THUNDER fluorescence microscope, and representative images were prepared in FIJI before quantification using a custom CellProfiler pipeline.[73, 74] The diameter of individual microgels was calculated as the diameter of a circle with equivalent area. Microgel deformation (D) was calculated using Equation 1:

$$D = \frac{1 - \left(\frac{a}{b}\right)}{1 + \left(\frac{a}{b}\right)} \qquad (1)$$

where a and b are the minor and major axes of the microgel, respectively.[47, 48] The microgel aspect ratio was calculated by dividing the major axis of the microgel (b) by its minor axis (a).

***3D Printing of GelMA and AlgOx Microgel Inks*:** Each microgel type was freshly jammed in preparation for 3D printing. AlgOx microgels were sedimented via gravity, and the liquid phase was removed using a micropipette. GelMA microgels were jammed using a vacuum-driven filtration unit (Nalgene™ Rapid-Flow™). Jammed slurries of GelMA and AlgOx microgels were mixed by weight to produce microgel blend inks with different ratios of GelMA to AlgOx microgel content. The inks were then thoroughly mixed and loaded into a 2.5 mL glass gastight syringe (Hamilton) fitted with a 20-gauge tapered dispensing nozzle (ID = 630 µm; Jensen

Global). 3D printing was performed using a MakerGear M2 Rev E plastic 3D printer modified to allow two-material bioprinting.[5, 75, 76] Lattice structures used for shape fidelity assessment were 15 mm by 15 mm and composed of two perpendicularly stacked layers. Disks used for void fraction quantification and cell culture were 8 mm in diameter and 1 mm in height. Tool paths for lattices were generated by hand, while tool paths for disks were created using Fusion360 (Autodesk) and sliced using Slic3r.[77] Inks were stored on ice, and the structures were printed at room temperature to limit unwanted GelMA microgel melting before UV crosslinking. After 3D printing, constructs were crosslinked under a UV lamp (wavelength = 365 nm) for 5 min before incubation in DPBS at 37 °C.

***Assessment of GelMA and AlgOx Microgel Ink Extrudability and Stability*:** The extrudability of eleven ink formulations ranging from 100% GelMA (100:0) to 100% AlgOx (0:100) was assessed by measuring the maximum hanging filament length upon extrusion through a 20-gauge tapered nozzle (ID = 600 μm; Jensen Global).[58] Approximately 1.5 mL of each ink was prepared as described, and the printing syringe was loaded into the 3D printer. The ink was extruded in small increments (extrusion command, E = 0.1) while recording a video. The entire volume of each ink was extruded to monitor changes in filament length throughout extrusion. Each extrusion video was used to extract images of individual hanging filaments immediately before filament breakage. Filament length was quantified using FIJI.[73]

The stability of UV-crosslinked GelMA:AlgOx inks was assessed using cast disks of each ink. After UV crosslinking, the samples were incubated in DPBS containing 1 mg mL^{-1} FITC-Dextran for 1 day at 37 °C to observe stability. Finally, ethylenediaminetetraacetic acid (EDTA; Invitrogen) was added to 0.5 м to ensure complete AlgOx microgel dissolution, after which samples were physically inspected and photographed.

***Rheological Characterization of GelMA and AlgOx Microgel Inks*:** An ARG2 stress-controlled rheometer equipped with a 20 mm parallel plate geometry was used to measure the rheological properties of uncrosslinked GelMA:AlgOx inks with microgel ratios ranging from 100:0 to 50:50. Samples were prepared as described and loaded into a 2.5 mL gastight syringe (Hamilton) fitted with a 20-gauge tapered nozzle (ID = 600 μm; Jensen Global). Approximately 500 μL of each ink was extruded onto the rheometer stage, and the gap height was set to 1.5 mm. All tests were performed at 23 °C. For inks that demonstrated extrusion-mediated compaction, only the extrudable phase (i.e., the final ~30% of prepared volume) was used for rheological and subsequent testing. The linear viscoelastic region was investigated by performing a frequency amplitude sweep over a range of 0.01 to 1,000 Hz with 1% strain. Storage moduli were determined by performing time-sweep experiments for 2.5–5 min each at 1 Hz and 1% strain. Yielding behavior was assessed by subjecting samples to shear strain-sweep experiments over a range of 0.01 to 1,000% strain at a frequency of 1 Hz. The viscosity was measured using a range of shear rates from 0.01 to 100 s^{-1}. To assess ink self-healing, the samples were subjected to alternating periods of high and low shear stress. These shear stress values were determined to be above (high) and below (low) the *G′/G″* crossover point after conducting a shear stress-sweep experiment over a range of 0.01 to 1,000 Pa at 1 Hz and 1% strain.

***Assessment of Lattice Shape Fidelity*: ** The printability of GelMA:AlgOx microgel inks was further investigated qualitatively and quantitatively by evaluating the shape fidelity of a printed lattice.[18] Specifically, the retention and shape of the square, open windows formed by the lattice were monitored for unwanted material spreading or deformation. After printing, lattice structures made from GelMA and FITC-containing AlgOx microgels were imaged using a Leica THUNDER fluorescence microscope with a tile scan function. Images were processed, and window measurements were conducted in FIJI.[73] The ink spreading (*Sp*) and window printability (Pr_W) were determined using Equations 2 and 3, respectively:

$$Sp = \frac{A_t - A_a}{A_t} \times 100\% \tag{2}$$

$$Pr_W = \frac{P^2}{16\,A_a} \tag{3}$$

where A_t and A_a are the theoretical and actual areas of the printed window, respectively, and P is the perimeter of the window.[18, 62-64] For an ink with ideal shape fidelity, which forms perfectly square windows, $Sp = 0$ (i.e., $A_t = A_a$) and $Pr_W = 1$. Plotted values represent measurements from the fully enclosed windows (up to 36) of a representative lattice for each GelMA:AlgOx microgel ink.

The homogeneous distribution of AlgOx microgels within printed lattices was confirmed using FITC-containing AlgOx microgels. Tile scans produced during shape fidelity testing were used to quantify fluorescence intensity across four vertical struts and the three enclosed lattice windows. Representative images were prepared, and analysis was performed in FIJI.[73]

***Quantification of Void Fraction within GelMA and AlgOx Microgel Inks*:** UV-crosslinked disks (8 mm x 1 mm) 3D printed using each GelMA:AlgOx microgel ink were incubated in DPBS containing 1 mg mL^{-1} 2,000-kDa FITC-dextran (Sigma-Aldrich) and 50 mᴍ EDTA (Invitrogen) for 1 h at 37 °C to fill the void space between GelMA microgels and dissociate the sacrificial AlgOx microgels. The labeled samples were then imaged using a Leica STELLARIS 5 confocal microscope to obtain *z*-stacks with a height of at least 150 µm. The total void volume was measured as a fraction of the total volume represented by the *z*-stack and was quantified using a custom CellProfiler pipeline.[74] A minimum of nine measurements were taken for each microgel ratio. Representative images were prepared in FIJI.[73]

***HUVEC Expansion and Encapsulation within AlgOx Microgels*:** Human umbilical vein endothelial cells (HUVEC, C2519A; Lonza) were expanded in endothelial growth medium-2 (EGM-2; Lonza), and the culture medium was changed every other day. In preparation for encapsulation, HUVEC were briefly washed two times with DPBS (Corning), incubated for 5 min in 0.05% Trypsin-EDTA (Gibco), collected with EGM-2 supplemented with 10% fetal bovine serum (FBS), centrifuged for 4 min at 1000 rpm, and resuspended to count. A solution of 2 wt% AlgOx with 10^7 cells mL^{-1} was prepared in EGM-2 and used to fabricate cell-containing AlgOx microgels as described. After collection, HUVEC-laden AlgOx microgels were used for 3D printing. 3D printed and UV-crosslinked, HUVEC-laden GelMA:AlgOx inks were rinsed thrice in DPBS and once every other day to aid AlgOx dissolution. HUVEC viability was assessed prior to encapsulation using a Countess 3 automated cell counter. After encapsulation, the viability of HUVEC within AlgOx microgels was characterized using a Live/Dead™ staining kit (Life Technologies). Briefly, live (calcein AM) and dead (ethidium homodimer-1) stains were diluted in HBSS according to the manufacturer's protocol, and AlgOx microgels containing HUVEC were resuspended in the staining solution. Samples were incubated for 15 min, pipetted onto a coverslip, and imaged using a Leica STELLARIS 5 confocal microscope. A custom CellProfiler pipeline was used to measure the number of cells with intact (live) or damaged (dead) membranes, and representative images were prepared in FIJI.[73, 74]

***Visualizing Cell Morphology and Quantification of Cell Distribution*:** Cell-laden GelMA:AlgOx bioinks were 3D bioprinted into disks and UV-crosslinked as described above. After 7 days in culture, a portion of the HUVEC-laden disks were stained using calcein AM to label cell bodies. Stained samples were imaged using a Leica STELLARIS 5 confocal microscope, and representative images were prepared in FIJI.[73] Next, HUVEC nuclei and actin cytoskeleton were stained to visualize cell location. The remaining samples were fixed with 4% paraformaldehyde (PFA; Electron Microscopy Sciences) in DPBS for 45 min at 37 °C, followed by permeabilization and blocking of nonspecific binding for 1 h at room temperature in DPBS containing 0.25% Triton X-100 (DPBST; Sigma-Aldrich) and 1 wt% bovine serum albumin (BSA; Roche). The cell nucleus and actin cytoskeleton were then stained through incubation with 4',6-diamidino-2-phenylindole dihydrochloride (DAPI, 1:2000; Cell Signaling Technology) and tetramethylrhodamine (TRITC)-labeled phalloidin (1:200; Sigma-Aldrich) in DPBST for 1 h at room temperature. Samples were washed with DPBST and imaged using a Leica STELLARIS 5 confocal microscope ($n = 9$). Nuclear z-position was quantified using a custom CellProfiler pipeline, and representative images were prepared in FIJI.[73, 74]

Statistical Analysis**:** All statistical analyses and plotting were performed using GraphPad Prism 9.0. In vitro experiments had at least three independent gel samples for each condition. Statistical significance was assessed using an unpaired t test (two conditions) or a one-way ANOVA with Tukey post hoc test (three or more conditions). All errors are reported as the standard deviation (*SD*) unless otherwise noted.

Supporting Information

Supporting Information is available online or from the author.

Acknowledgements

The authors acknowledge Sungchul Shin and Aidan Gilchrist for consultation on GelMA synthesis. Additionally, S.C.H. acknowledges financial support from the National Science Foundation (DMR 2103812 and CBET 2033302) and the National Institutes of Health (R01 HL142718, R01 EB027666, R01 EB027171, and R01 HL151997). S.M.H. acknowledges support from an NIH NRSA pre-doctoral fellowship (F31 EY030731) and a Stanford Bio-X Interdisciplinary Graduate Fellowship. R.S.N acknowledges support from the American Heart Association postdoctoral fellowship (903771).

References

1. C. Mandrycky, Z. Wang, K. Kim and D.-H. Kim, *Biotechnology Advances*, 2016, **34**, 422-434.
2. A. J. Seymour, A. D. Westerfield, V. C. Cornelius, M. A. Skylar-Scott and S. C. Heilshorn, *Biofabrication*, 2022, **14**, 022002-022002.
3. M. A. Skylar-Scott, S. G. M. Uzel, L. L. Nam, J. H. Ahrens, R. L. Truby, S. Damaraju and J. A. Lewis, *Science advances*, 2019, **5**, eaaw2459-eaaw2459.
4. A. C. Daly, M. D. Davidson and J. A. Burdick, *Nature Communications*, 2021, **12**, 1-13.
5. A. Lee, A. R. Hudson, D. J. Shiwarski, J. W. Tashman, T. J. Hinton, S. Yerneni, J. M. Bliley, P. G. Campbell and A. W. Feinberg, *Science*, 2019, **365**, 482-487.
6. J. Groll, J. A. Burdick, D. w. Cho, B. Derby, M. Gelinsky, S. C. Heilshorn, T. Jüngst, J. Malda, V. A. Mironov, K. Nakayama, A. Ovsianikov, W. Sun, S. Takeuchi, J. J. Yoo and T. B. F. Woodfield, *Biofabrication*, 2018, **11**, 013001-013001.
7. S. M. Hull, L. G. Brunel and S. C. Heilshorn, *Advanced Materials*, 2022, **34**, 1-17.
8. A. Schwab, R. Levato, M. D'Este, S. Piluso, D. Eglin and J. Malda, *Chemical Reviews*, 2020, **120**, 11028-11055.
9. J. Malda, J. Visser, F. P. Melchels, T. Jüngst, W. E. Hennink, W. J. A. Dhert, J. Groll and D. W. Hutmacher, *Advanced Materials*, 2013, **25**, 5011-5028.
10. A. C. Daly, L. Riley, T. Segura and J. A. Burdick, *Nature Reviews Materials*, 2020, **5**, 20-43.
11. L. Riley, L. Schirmer and T. Segura, *Current Opinion in Biotechnology*, 2019, **60**, 1-8.
12. C. B. Highley, K. H. Song, A. C. Daly and J. A. Burdick, *Advanced Science*, 2019, **6**, 1801076-1801076.
13. T. H. Qazi and J. A. Burdick, *Biomaterials and Biosystems*, 2021, **1**, 100008-100008.
14. J. P. Newsom, K. A. Payne and M. D. Krebs, *Acta Biomaterialia*, 2019, **88**, 32-41.
15. J. M. de Rutte, J. Koh and D. Di Carlo, *Advanced Functional Materials*, 2019, **29**.
16. D. R. Griffin, W. M. Weaver, P. O. Scumpia, D. Di Carlo and T. Segura, *Nature Materials*, 2015, **14**, 737-744.
17. N. F. Truong, E. Kurt, N. Tahmizyan, S. C. Lesher-Pérez, M. Chen, N. J. Darling, W. Xi and T. Segura, *Acta Biomaterialia*, 2019, **94**, 160-172.
18. A. J. Seymour, S. Shin and S. C. Heilshorn, *Advanced Healthcare Materials*, 2021, **10**, 2100644-2100644.
19. L. Shao, Q. Gao, C. Xie, J. Fu, M. Xiang, Z. Liu, L. Xiang and Y. He, *Bio-Design and Manufacturing*, 2020, **3**, 30-39.
20. A. Sheikhi, J. deRutte, R. Haghniaz, O. Akouissi, A. Sohrabi, D. DiCarlo and A. Khademhosseini, *Biomaterials*, 2019, **192**.
21. O. Y. Dudaryeva, A. Bucciarelli, G. Bovone, F. Huwyler, S. Jaydev, N. Broguiere, M. al‐Bayati, M. Lütolf and M. W. Tibbitt, *Advanced Functional Materials*, 2021, **31**.
22. A. G. Guex, J. L. Puetzer, A. Armgarth, E. Littmann, E. Stavrinidou, E. P. Giannelis, G. G. Malliaras and M. M. Stevens, *Acta Biomater*, 2017, **62**, 91-101.
23. B. D. Ratner, *Regenerative Biomaterials*, 2016, **3**, 107-110.
24. A. S. Caldwell, G. T. Campbell, K. M. T. Shekiro and K. S. Anseth, *Adv Healthc Mater*, 2017, **6**.
25. A. C. Suturin, A. J. D. Kruger, K. Neidig, N. Klos, N. Dolfen, M. Bund, T. Gronemann, R. Sebers, A. Manukanc, G. Yazdani, Y. Kittel, D. Rommel, T. Haraszti, J. Kohler and L. De Laporte, *Adv Healthc Mater*, 2022, **11**, e2200989.
26. T. H. Qazi, J. Wu, V. G. Muir, S. Weintraub, S. E. Gullbrand, D. Lee, D. Issadore and J. A. Burdick, *Advanced Materials*, 2022, **34**, 2109194-2109194.

27. B. Kessel, M. Lee, A. Bonato, Y. Tinguely, E. Tosoratti and M. Zenobi ‐ Wong, *Advanced Science*, 2020, **7**, 2001419-2001419.
28. A. R. Anderson, E. Nicklow and T. Segura, *Acta Biomaterialia*, 2022, **150**, 111-127.
29. D. R. Griffin, M. M. Archang, C. H. Kuan, W. M. Weaver, J. S. Weinstein, A. C. Feng, A. Ruccia, E. Sideris, V. Ragkousis, J. Koh, M. V. Plikus, D. Di Carlo, T. Segura and P. O. Scumpia, *Nat Mater*, 2021, **20**, 560-569.
30. L. R. Nih, E. Sideris, S. T. Carmichael and T. Segura, *Advanced Materials*, 2017, **29**, 1-8.
31. S. Xin, D. Chimene, J. Garza, A. Gaharwar and D. Alge, *Biomaterials Science*, 2019, **7**.
32. M. Zhong, D. Wei, Y. Yang, J. Sun, X. Chen, L. Guo, Q. Wei, Y. Wan, H. Fan and X. Zhang, *ACS Appl Mater Interfaces*, 2017, **9**, 3524-3534.
33. O. Jeon, Y. B. Lee, T. J. Hinton, A. W. Feinberg and E. Alsberg, *Materials Today Chemistry*, 2019, **12**, 61-70.
34. W. Liu, M. A. Heinrich, Y. Zhou, A. Akpek, N. Hu, X. Liu, X. Guan, Z. Zhong, X. Jin, A. Khademhosseini and Y. S. Zhang, *Adv Healthc Mater*, 2017, **6**.
35. H. Shirahama, B. H. Lee, L. P. Tan and N.-J. Cho, *Scientific Reports*, 2016, **6**, 31036-31036.
36. A. I. Van Den Bulcke, B. Bogdanov, N. De Rooze, E. H. Schacht, M. Cornelissen and H. Berghmans, *Biomacromolecules*, 2000, **1**, 31-38.
37. V. G. Muir, T. H. Qazi, J. Shan, J. Groll and J. A. Burdick, *ACS Biomaterials Science & Engineering*, 2021, **7**, 4269-4281.
38. V. G. Muir, T. H. Qazi, S. Weintraub, B. O. Torres Maldonado, P. E. Arratia and J. A. Burdick, *Small*, 2022, **18**, 2201115-2201115.
39. J. A. Rowley, G. Madlambayan and D. J. Mooney, *Biomaterials*, 1999, **20**, 45-53.
40. K. H. Bouhadir, K. Y. Lee, E. Alsberg, K. L. Damm, K. W. Anderson and D. J. Mooney, *Biotechnology Progress*, 2001, **17**, 945-950.
41. O. Chaudhuri, L. Gu, D. Klumpers, M. Darnell, S. A. Bencherif, J. C. Weaver, N. Huebsch, H. P. Lee, E. Lippens, G. N. Duda and D. J. Mooney, *Nature Materials*, 2016, **15**, 326-334.
42. L. Malaprade, *Comptes Rendus*, 1928, **186**, 382-384.
43. L. Malaprade, *Bulletin de la Societe Chimique de France*, 1928, **43**, 683-696.
44. T. Boontheekul, H.-J. Kong and D. J. Mooney, *Biomaterials*, 2005, **26**, 2455-2465.
45. K. A. Kristiansen, H. B. Tomren and B. E. Christensen, *Carbohydrate Polymers*, 2011, **86**, 1595-1601.
46. O. Jeon, D. S. Alt, S. M. Ahmed and E. Alsberg, *Biomaterials*, 2012, **33**, 3503-3514.
47. S.-M. Kang, G.-W. Lee and Y. S. Huh, *Scientific Reports*, 2019, **9**, 12776-12776.
48. K. Maeda, H. Onoe, M. Takinoue and S. Takeuchi, *Advanced Materials*, 2012, **24**, 1340-1346.
49. L. H. Han, J. H. Lai, S. Yu and F. Yang, *Biomaterials*, 2013, **34**, 4251-4258.
50. M. L. Moya, M. Morley, O. Khanna, E. C. Opara and E. M. Brey, *J Mater Sci Mater Med*, 2012, **23**, 903-912.
51. K. Y. Lee and D. J. Mooney, *Progress in Polymer Science (Oxford)*, 2012, **37**, 106-126.
52. W. H. Tan and S. Takeuchi, *Advanced Materials*, 2007, **19**, 2696-2701.
53. S. Utech, R. Prodanovic, A. S. Mao, R. Ostafe, D. J. Mooney and D. A. Weitz, *Adv Healthc Mater*, 2015, **4**, 1628-1633.
54. J. L. Madrigal, S. N. Sharma, K. T. Campbell, R. S. Stilhano, R. Gijsbers and E. A. Silva, *Acta Biomaterialia*, 2018, **69**, 265-276.
55. C. A. Verheyen, S. G. M. Uzel, A. Kurum, E. T. Roche and J. A. Lewis, *Matter*, 2023, DOI: 10.1016/j.matt.2023.01.011.
56. L. Ouyang, J. P. K. Armstrong, Q. Chen, Y. Lin and M. M. Stevens, *Advanced Functional Materials*, 2020, **30**.

57. M. Xie, Y. Sun, J. Wang, Z. Fu, L. Pan, Z. Chen, J. Fu and Y. He, *Int J Bioprint*, 2022, **8**, 599.
58. S. Xin, K. A. Deo, J. Dai, N. K. R. Pandian, D. Chimene, R. M. Moebius, A. Jain, A. Han, A. K. Gaharwar and D. L. Alge, *Science Advances*, 2021, **7**.
59. D. B. Emiroglu, A. Bekcic, D. Dranseikiene, X. Zhang, T. Zambelli, A. J. deMello and M. W. Tibbitt, *Sci Adv*, 2022, **8**, eadd8570.
60. F. Scheffold, *Nat Commun*, 2020, **11**, 4315.
61. G. Gillispie, P. Prim, J. Copus, J. Fisher, A. G. Mikos, J. J. Yoo, A. Atala and S. J. Lee, *Biofabrication*, 2020, **12**, 022003-022003.
62. L. Ouyang, R. Yao, Y. Zhao and W. Sun, *Biofabrication*, 2016, **8**, 035020-035020.
63. A. Habib, V. Sathish, S. Mallik and B. Khoda, *Materials*, 2018, **11**.
64. Y. He, F. Yang, H. Zhao, Q. Gao, B. Xia and J. Fu, *Scientific Reports*, 2016, **6**, 29977-29977.
65. A. J. Liu and S. R. Nagel, *Annual Review of Condensed Matter Physics*, 2010, **1**, 347-369.
66. N. J. Darling, W. Xi, E. Sideris, A. R. Anderson, C. Pong, S. T. Carmichael and T. Segura, *Advanced Healthcare Materials*, 2020, **9**, 1901391-1901391.
67. T. Distler, K. McDonald, S. Heid, E. Karakaya, R. Detsch and A. R. Boccaccini, *ACS Biomaterials Science & Engineering*, 2020, **6**, 3899-3914.
68. S. Mascharak, P. L. Benitez, A. C. Proctor, C. M. Madl, K. H. Hu, R. E. Dewi, M. J. Butte and S. C. Heilshorn, *Biomaterials*, 2017, **115**, 155-166.
69. C. A. Reinhart-King, M. Dembo and D. A. Hammer, *Biophysical Journal*, 2005, **89**, 676-689.
70. S. Xin, J. Dai, C. A. Gregory, A. Han and D. L. Alge, *Advanced Functional Materials*, 2019, **30**.
71. S. Reakasame and A. R. Boccaccini, *Biomacromolecules*, 2018, **19**, 3-21.
72. J. Vasudevan, C. T. Lim and J. G. Fernandez, *Advanced Functional Materials*, 2020, **30**.
73. J. Schindelin, I. Arganda-Carreras, E. Frise, V. Kaynig, M. Longair, T. Pietzsch, S. Preibisch, C. Rueden, S. Saalfeld, B. Schmid, J. Y. Tinevez, D. J. White, V. Hartenstein, K. Eliceiri, P. Tomancak and A. Cardona, *Nat Methods*, 2012, **9**, 676-682.
74. C. McQuin, A. Goodman, V. Chernyshev, L. Kamentsky, B. A. Cimini, K. W. Karhohs, M. Doan, L. Ding, S. M. Rafelski, D. Thirstrup, W. Wiegraebe, S. Singh, T. Becker, J. C. Caicedo and A. E. Carpenter, *PLOS Biology*, 2018, **16**, e2005970-e2005970.
75. S. M. Hull, C. D. Lindsay, L. G. Brunel, D. J. Shiwarski, J. W. Tashman, J. G. Roth, D. Myung, A. W. Feinberg and S. C. Heilshorn, *Advanced Functional Materials*, 2021, **31**, 2007983-2007983.
76. K. Pusch, T. J. Hinton and A. W. Feinberg, *HardwareX*, 2018, **3**, 49-61.
77. Slic3r, Slic3r - Open source 3D printing toolbox, https://slic3r.org).